Computers in Biology and Medicine 180 (2024) 108862

Contents lists available at ScienceDirect

Computers in Biology and Medicine

journal homepage: www.elsevier.com/locate/compbiomed

$^{\mathcal{R}}$SCZ: A Riemannian schizophrenia diagnosis framework based on the multiplexity of EEG-based dynamic functional connectivity patterns

Stavros I. Dimitriadis [a,b,c,d,*]

[a] Department of Clinical Psychology and Psychobiology, University of Barcelona, Passeig Vall D'Hebron 171, 08035, Barcelona, Spain
[b] Institut de Neurociencies, University of Barcelona, Municipality of Horta-Guinardó, 08035, Barcelona, Spain
[c] Integrative Neuroimaging Lab, Thessaloniki, 55133, Makedonia, Greece
[d] Neuroinformatics Group, Cardiff University Brain Research Imaging Centre (CUBRIC), School of Psychology, College of Biomedical and Life Sciences, Cardiff University, Maindy Rd, CF24 4HQ, Cardiff, Wales, United Kingdom

ARTICLE INFO

Keywords:
EEG
Schizophrenia
Dynamic functional connectivity analysis
Multiplexity
Riemannian geometry
Biomarkers
Default mode network

ABSTRACT

Abnormal electrophysiological (EEG) activity has been largely reported in schizophrenia (SCZ). In the last decade, research has focused to the automatic diagnosis of SCZ via the investigation of an EEG aberrant activity and connectivity linked to this mental disorder. These studies followed various preprocessing steps of EEG activity focusing on frequency-dependent functional connectivity brain network (FCBN) construction disregarding the topological dependency among edges. FCBN belongs to a family of symmetric positive definite (SPD) matrices forming the Riemannian manifold. Due to its unique geometric properties, the whole analysis of FCBN can be performed on the Riemannian geometry of the SPD space. The advantage of the analysis of FCBN on the SPD space is that it takes into account all the pairwise interdependencies as a whole. However, only a few studies have adopted a FCBN analysis on the SPD manifold, while no study exists on the analysis of dynamic FCBN (dFCBN) tailored to SCZ. In the present study, I analyzed two open EEG-SCZ datasets under a Riemannian geometry of SPD matrices for the dFCBN analysis proposing also a multiplexity index that quantifies the associations of multi-frequency brainwave patterns. I adopted a machine learning procedure employing a leave-one-subject-out cross-validation (LOSO-CV) using snapshots of dFCBN from (N-1) subjects to train a battery of classifiers. Each classifier operated in the inter-subject dFCBN distances of sample covariance matrices (SCMs) following a rhythm-dependent decision and a multiplex-dependent one. The proposed $^{\mathcal{R}}$**SCZ** decoder supported both the Riemannian geometry of SPD and the multiplexity index DC reaching an absolute accuracy (100 %) in both datasets in the virtual default mode network (DMN) source space.

1. Introduction

Schizophrenia (SCZ) is a chronic and debilitating psychiatric illness that is accompanied by positive and negative symptoms. As positive symptoms are categorized the psychotic symptoms, such as delusions of persecution and auditory hallucinations [1]. Negative symptoms include low motivation, diminished verbal and/or non-verbal expression, and cognitive dysfunction that may precede the emergence of positive symptoms [2]. In SCZ, the distinction between positive, and negative symptoms corresponds to clinical observations, originated in the field of neurology, and allows the clinicians to describe the disorder in terms of symptoms. Positive symptoms of SCZ reflect an excess of normal function (eg, delusions, hallucinations, disorganized behavior), while negative symptoms refer to absence of normal behaviors related to motivation and interest (eg, avolition, anhedonia, asociality) or expression (eg, blunted affect, alogia). Negative symptoms are a core component of SCZ and they account for a large part of the long-term morbidity and poor functional outcome in patients with the disorder [3–5]. They are associated with deficiencies in motivation, communication, and social functioning, encapsulating a multifaceted concept with dimensions that impact the functional outcome [6].

Positive symptoms are effectively managed with available antipsychotic medications. However, limited treatment options are available for negative symptoms and despite advances in understanding the epidemiology, etiology, biology, and psychopharmacology of SCZ, they remain an unmet medical need [7,8].

SCZ patients show abnormalities in personality [9], cognition [10], visual perception [11], and immunology [12]. SCZ has a high disability, incidence, and recurrence rate among young adults [13]. Disability is

* Department of Clinical Psychology and Psychobiology, University of Barcelona, Passeig Vall d'Hebron 171, 08035, Barcelona, Spain.
E-mail address: stidimitriadis@gmail.com.

https://doi.org/10.1016/j.compbiomed.2024.108862
Received 11 February 2024; Received in revised form 30 June 2024; Accepted 6 July 2024
Available online 27 July 2024
0010-4825/© 2024 The Author. Published by Elsevier Ltd. This is an open access article under the CC BY license (http://creativecommons.org/licenses/by/4.0/).

Abbreviations

SCZ	Schizophrenia
DC	distance correlation
PCC	Pearson's correlation coefficient
FCBN	functional connectivity brain network
dFCBN	dynamic functional connectivity brain network
rs-FCBN	resting-state dynamic FCBN
SSD	schizophrenia spectrum disorders
MDRM	Minimum Distance to Riemannian Mean
TSA	Tensor Subspace Analysis
k-NN	k-nearest-neighbors
LDA	linear discriminative analysis
SVM	support vector machines
DMN	default mode network
LOSO-CV	leave-one-out subject cross-validation scheme
SPD	symmetric positive definite
SCM	sample covariance matrices
EEG	electroencephalography
MEG	magnetoencephalography
MRI	magnetic resonance imaging
fMRI	functional magnetic resonance imaging
PET	positron emission tomography
ML	machine learning
DL	deep learning
NMDA	N-methyl-D-aspartate receptor
BCI	brain-computer interface
PLV	phase locking value
AIRM	affine-invariant Riemannian metric
LERM	log-Euclidean Riemannian metric

any lack of ability to perform an activity within the range that is considered normal for a human being [14]. Positive-negative symptoms and cognitive deficits are some of the core aspects determining functional and vocational outcomes in SCZ. Cognitive impairment is one of the core aspects of SCZ which is the key determinant of functional and vocational outcomes [15]. Disability in SCZ can affect functioning in important daily activities such as occupational performance, interaction with family members, self-care, and socialization [16]. Worldwide, it is one of the leading causes of years lost due to disability in males and females [17]. SCZ affects approximately 1 % of the world's population (~20–24 million people) which causes a global public health burden [18,19].

Detecting SCZ using machine learning (ML), and deep learning (DL) techniques incorporating proper advanced signal processing methods is a significant research area which can make a great impact on improving early diagnosis of SCZ and adaptive intervention tailored to SCZ symptoms. ML/DL techniques can analyze in general various sources of data, including biomedical signals like recordings from electroencephalography (EEG), to identify patterns and important markers associated to SCZ [20]. The neuroscience community should urgently design a reliable method to detect the subjects with SCZ, an important step towards an early diagnosis of this mental disorder. The potential methodological framework could improve the lives of the patients by designing and applying interventions tailored to SCZ while reducing the public health burden of society [21].

Our understanding of how brain functions or dysfunctions has developed considerably since the born of cognitive neuroscience and functional neuroimaging. Apparently, there are two central principles that govern functional brain architectures: functional specialization and functional integration. The former posits that brain systems are specialized for various perceptual and cognitive functions, while the latter underlines the interactions among these specialized systems [22]. This integration is mediated by the functional connectivity (defined as the functional coupling of the activity or dynamics of one neuronal system with the activity or dynamics of the other). The notion of functional connectivity released the disconnection hypothesis, which was an attempt to understand SCZ via mechanistic terms. The idea that dysfunctional integration underlies SCZ is as old as its name, first represented by Bleuler [23] as a way to define the disintegration of psychic processes. The disconnection hypothesis states that SCZ can be understood in both cognitive and pathophysiological terms, as a failure of functional integration within the brain. Functional integration refers to the interactions of functionally specialized systems like cortical areas and sub-areas, that are required for adaptive sensorimotor integration, perceptual synthesis and cognition as a demanding daily request to various stimuli. Functional integration is mediated by the functional coupling strength between the dynamics or activity between neuronal systems and therefore rests on the connections among them.

Functional dysconnectivity in the brain in general and specifically in SCZ can be seen in two ways: as impaired functional specialization or as a dysfunctional integration. This practically means that there is an important distinction between the pathological interaction of two cortical brain areas and the alternative normal interaction of two pathological brain areas. In other words, the symptoms and signs of SCZ do not generally represent a single deficit, but can be seen as resulting from the abnormal integration of two or more processes. Similarly, the disconnection hypothesis suggests that the neuronal dynamics underlying these symptoms are not due to a single regionally specific pathophysiology, but are expressed when two or more regions interact [24].

The key assumption here is that the pathophysiology of SCZ is expressed in terms of abnormal connections. To understand functional disconnection, in its broadest sense, one has to appreciate the diversity of mechanisms that are responsible for establishing connections in the normal brain. In summary, there are two basic determinants of connectivity in the brain: a) structural plasticity, which refers to neurodevelopmental interactions between gene expressions, neurogenesis, cell migration, b) synaptic plasticity, i.e., activity-dependent modelling of the pattern and strength of synaptic connections which is changed across the life due to learning and memory processing [25].

Psychosis can be induced by changes on the neuromodulatory status of synaptic integration suggesting that aberrant anatomical, functional and neurodevelopmental characteristics of SCZ are the consequences and not the causes of the pathophysiology [26]. The dysconnection hypothesis attempts to establish a link between the symptoms and signs of SCZ with the underlying molecular and neuronal pathophysiology. It supports that psychosis is best understood – at a systems level – in terms of aberrant neuromodulation of synaptic efficacy that mediates the context-sensitive influence of intrinsic and extrinsic long-range functional connectivity [24]. This disconnection hypothesis proposes that the key pathophysiology lies in the interactions between NMDA receptor[1] function and modulatory neurotransmitter systems [27].

Motivated by the aforementioned hypothesis, and relevant supporting findings, many research studies focused on the investigation of how structural (anatomical), and functional/effective connectivity is altered in SCZ group compared to age-matched healthy controls [28–30]. Structural and functional neuroimaging investigations in SCZ have produced a large body of evidences for both structural and functional abnormalities associated with the SCZ. It is clear from the literature review that there is a high variability on the findings linked to white matter tracts [31], on various metrics estimated from EEG signals [20],

[1] **N-methyl-D-aspartate** receptor is a glutamate receptor and predominantly Ca^{2+} ion channel found in neurons.

and also on functional magnetic resonance imaging (fMRI) recordings [30,32]. Several factors contribute to the inconsistent findings including variability in the clinical presentation of schizophrenia, methodological differences between studies, variation to moderator variables across studies, the analysis of private datasets to name a few. This variability in results is evident even on studies analyzed the same dataset, while the major source of this variability at this case is related to the adopted preprocessing steps, and statistical analysis (pipeline) [33].

Over the last two decades, numerous neuroimaging techniques have been widely used on the investigation of sensitive biomarkers for the detection and diagnosis of SCZ. The most frequent used neuroimaging modalities are diffusion tensor imaging [34], magnetic resonance spectroscopy [35], magnetic resonance imaging (MRI) [31], functional magnetic resonance imaging (fMRI) [32], magnetoencephalography (MEG) [36], and electroencephalography (EEG) [20]. However, EEG attracted too much attention from many research groups due to advantageous features of this modality such as: the low-cost, non--invasiveness, the portability compared to medical-imaging techniques, and its overall sensitivity to detect aberrant activity in SCZ [20].

On the era of open science, three EEG SCZ datasets have been released by the research teams involved on the data acquisitions as a way to become accessible to other investigators. The first dataset is released from the Institute of Psychiatry and Neurology in Warsaw, Poland, and is openly accessible in the RepOD dataset [37]. The second dataset originates from the Neurophysiology and Neuro-Computer Interfaces laboratory at the Mental Health Research Center (MHRC), Russia, and is publicly available [38]. The third and less-explored SCZ EEG dataset is collected under a project of the National Institute of Mental Health (NIMH; R01MH058262) and is publicly available on the Kaggle platform [39]. However, there are other EEG studies with private SCZ related datasets. Below, I performed a review of the main EEG research activity in SCZ with both private and open EEG datasets.

STables 1,2 summarize the main characteristics of the studies employing machine/deep learning, correspondingly for the detection of SCZ. The articles employed the first/second/third open datasets were the [40,41,42,43,44,45,46–48], [49–51], and [52,53,54], correspondingly. The rest of the studies involved on this review presented their analytic framework on a private EEG recording set. The majority of the studies analyzed EEG resting-state activity on the sensor level [40–44, 52–60,47,48,61–65,49–51], two in both sensor, and source space [45, 66], and two only on the source level [46,67]. The majority of the studies estimated statistical, entropic, and complexity measures over multichannel EEG recordings, another subset of studies followed a static functional connectivity analysis [40,59,60,45,46,64,67,50,51], while a single one selected a dynamic functional connectivity analysis on the sensor level [49]. Regarding the preprocessing of the multichannel EEG recordings only a small portion of studies proceeded with a denoising ICA [56,57,59,45,48,61–63,65,67], while the majority adopted either a bandpass filtering, a wavelet transform or other relevant digital signal processing technique to extract the brain frequencies [40,41,52,43,56, 58,53,60,44–47,66,49,50,61–65,67]. The repertoire of classifiers in combination with cross-validation schemes was high. The most frequent classifier were the support vector machines (SVM), the linear discriminative analysis (LDA), and the k-nearest neighbor classifier (k-NN) accompanied with a frequent 10-fold cross-validation across the subjects dimension. Not all the studies reported a proper feature selection, while a high number of studies followed a wrong supervised feature selection outside the cross-validation adopting a statistical set [52,43,57,53,45, 66,61,65]. This supervised feature selection strategy outside the cross-validation framework may result in overfitting of the model, and it is prohibitive in machine learning (ML). In addition, two studies employed a large number of features multiple times higher than the actual number of subjects which leads to the so-called curse of dimensionality, and again may result in the overfitting of the model [49,50]. STables 1 and 2 present a diverse set of methodologies applied in EEG multichannel analysis, offering insights into various preprocessing techniques and classification/validation methods. In conclusion, all the studies presented their findings using solely one dataset, either open or private, while only one study followed a denoising processing step, and a construction of frequency-dependent dynamic functional connectivity brain networks on the source level [49]. However, they estimated a large number of features (unreported, but can be estimated by their description which produced a feature vector of 14.880 features), that caused an overfitting of the models, and an overestimation of the performance [49].

My study relies on the advantage of investigating resting-state EEG functional connectivity brain networks (FCBN) because subjects don't need to perform any task which can be affected by various factors like attention as a consequence of low motivation or mind wandering [19]. The present study will focus on the analysis of resting-state dynamic FCBN (rs-dFCBN) at both the sensor and source levels [20] restricted on the default mode network (DMN) [68,69]. There are strong evidences of dissociated patterns in DMN subnetwork connectivity in major psychiatric disorders [69], and especially in SCZ [68].

In summary, the disconnection hypothesis presented aforementioned was validated on the extensive literature in SCZ using EEG resting-state recordings [40–67,70,71] which showed their sensitivity on the detection of SCZ (STables 1, and 2). Current literature needs an end-to-end approach that will include advanced signal processing steps, proper machine learning techniques, and validation, dynamic functional connectivity analysis, presentation in both sensor, and source level, focusing on the DMN, and testing it in more than one open EEG dataset. On the top, it is important to take the advantage of the multiplexity of brain frequencies under the brain connectivity framework [33], while the estimated FCBN should be processed under a Riemannian geometry rather than the Euclidean geometry.

The main aim of the present study is to introduce an end-to-end EEG-based decoder for detecting SCZ individuals by incorporating the Riemann geometry of SPD matrices in the analysis of dFCBN. The EEG time series describe the activity of various brain areas. The FCBN can be constructed by the adaptation of a proper connectivity estimator such as covariance, and cross-correlation matrices to measure functional interdependencies between pairs of these time series. These FCBN matrices belong to the family of SPD matrices and form a mathematical structure called Riemann manifold [72]. The analysis of FCBN can be realized on the Riemann manifold of the SPD space. The main motivation of the present study is supported by the following reasons: (i) EEG signals can be transformed to FCBN that are SPD matrices and are affected by EEG features and common analytic pipelines such as the non-stationarity of EEG signals, artifact contamination, variability across subjects and experimental time, and others [73], (ii) a few but increasing number of functional connectivity studies have been conducted on the space of SPD matrices [74–76], (iii) Riemannian geometry has been applied to the coordination of multiple brain areas [77,70], (iv) to the best of author's knowledge, despite the rapid growth of the field tailored to FCBN, Riemannian approach has not yet extensively been investigated in the context of clinical neuroscience, and especially in psychiatry [71], (v) how Riemannian geometry performs in both sensor and source space, (vi) how the performance of Riemann geometry is affected by connectivity estimators, and (vii) if the performance of Riemann geometry can be replicated in two independent EEG datasets [78,79].

The main contributions of my study in the literature of EEG in SCZ research were.

(i) to test the suitability of Riemann geometry for decoding aberrant resting-state activity due to SCZ,
(ii) to explore the importance of exploring frequency-dependent dFCBN SPD matrices for detecting the SCZ individuals,
(iii) to investigate a novel multiplexity index based on distance correlation (DC) as a proper amplitude-to-amplitude multiplex coupling index that quantifies how the whole set of studying

brain frequencies between two brain areas are functionally coupled [70],

(iv) to compare the classification performance of frequency-dependent dFCBN vs multiplex dFCBN to detect SCZ individuals in both Euclidean space, and Riemannian geometry,

(v) to compare the classification performance in both sensor and source whole space, and in targeted DMN, and also

(vi) to validate the consistency of the findings in two independent EEG datasets.

I took advantage of the positive outcome of previous studies that exploited the notion of Riemann geometry to introduce it in the context of a novel EEG-based decoder tailored to SCZ. Based on this, each EEG resting-state recording was segmented into temporal epochs building an individual dFCBN that was realigned in the SPD manifold. The whole process is repeated for every subject in each studying frequency band (from δ to low gamma), and also for the multiplex dFCBN approach in both sensor and source whole space. I also repeated the same analysis targeting the DMN on the virtual space. As a cross-validation scheme, I adopted a leave-one-subject-out validation scheme (LOSO-CV), where I employed (N-1) dFCBN for training and the target dFCBN for testing. For evaluating the decoding performance, I adopted the Minimum Distance to Riemannian Mean (MDRM) classifier [79]. The proposed Riemannian classifier was compared to a classification scheme operated on Euclidean space.

The remainder of this paper is organized as follows: Section 2 describes the basic knowledge of Riemannian geometry. Section 3 is dedicated to the methodology for formulating my ^{R}SCZ dynamic decoder. Section 4 presents the employed EEG datasets and the preprocessing steps followed, Section 5 is devoted to the obtained results, and Section 6 is dedicated to the discussion of the added value and limitations of the study and the future directions of this work.

2. Background

2.1. Riemannian geometry

Riemannian geometry explores smooth manifolds with the support of a proper Riemannian structure [80]. A Riemannian manifold is a smooth differential manifold which assigns the inner product of Euclidean space at the tangent space of any space on manifold M. A covariance matrix P can be produced by estimating the covariance between S time series. The covariance matrix $P \in \mathbb{R}^{nxn}$ lies in a space of a symmetric positive-definite (SPD) matrices as:

$$SPD(N) = S(N) \cap P(N)$$

where $S(N) = \{P \in \mathbb{R}^{NxN}, P = P^T\}$ is the space of symmetric matrices, and $P(N) = \{P \in \mathbb{R}^{NxN}, u^T P u > 0, \forall u \in \mathbb{R}^N\}$ is the space of positive-definite matrices.

2.2. Riemannian manifold

Briefly, a manifold $\mathcal{M}$ is a topological space that locally resembles Euclidean space at each point, while it is called smooth when transition maps are also smooth. A Riemannian manifold *(M,)* is a smooth manifold whose inner product *gp* on the tangent space for a point p varies smoothly. The family *gp* of inner products is called a Riemannian metric (or Riemannian metric tensor). It is important to underline that Riemannian manifold is not a vector space. That means, we should get used with the concept of distance that satisfies metric properties on the space that is locally Euclidean-alike but it is definitely not an Euclidean space.

A tangent space $T_p\mathcal{M}$ at any point $p \in \mathcal{M}$ is a set of tangent vectors, which are derivatives of curves crossing p (Fig. 1). When we state that a manifold is locally similar to Euclidean space, we refer to the tangent space and its properties as being a vector space. The space of symmetric positive-definite matrices with the use of a Riemannian metric is a differentiable manifold $\mathcal{M}$ [81].

2.3. Riemannian metric

The distance between any pair of points on the Riemannian manifold is the shortest path length along a smooth Riemannian manifold, which is called geodesic distance. To quantify the Riemannian distance between two symmetric positive-definite matrices $P_1, P_2 \in SPD(N)$, we have to define a proper Riemannian metric.

A commonly used Riemannian metric is the so-called affine invariant Riemannian metric (AIRM), δ_R :

$$\delta_R(P_1, P_2) = \left\|\log\left(P_1^{-1}P_2\right)\right\|_F = \left[\left[\sum_{i=1}^{N} log^2 n_i\right]\right]^{1/2} \quad (1)$$

where n_i are the real eigenvalues of $P_1^{-1}P_2$, and $[[]]_F$ is the Frobenius norm

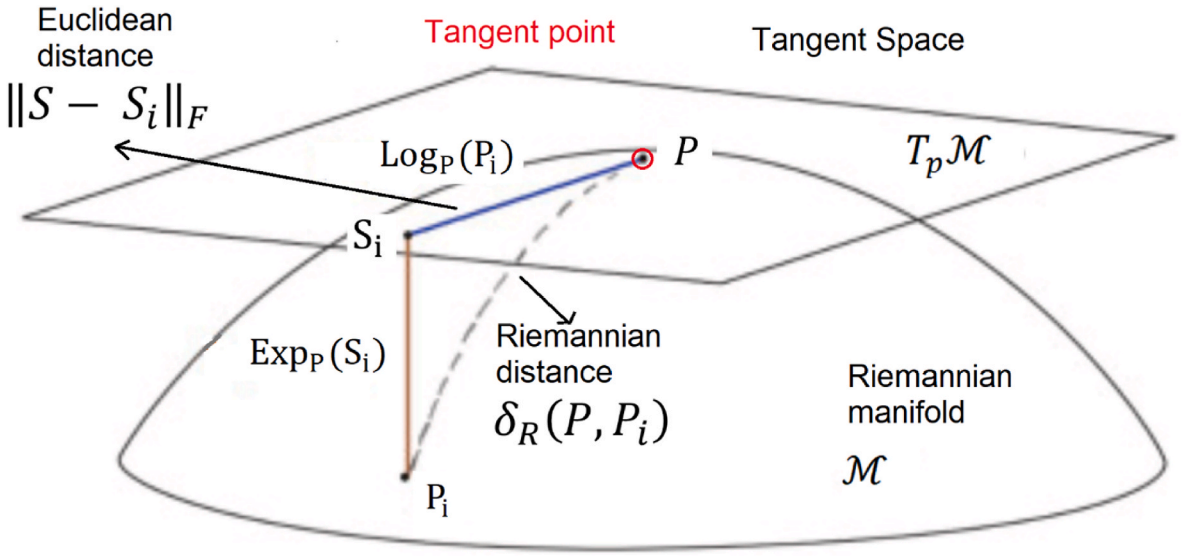

Fig. 1. Tangent space of the manifold Tp (M) at point M.
I showed the Riemannian manifold and its tangent space, while I defined both the Euclidean and Riemannian distance. Exponential map, and its inverse Logarithm map are also demonstrated.

of a matrix. The AIRM metric was proposed by Forstner and Moonen [81], and Pennec [82] who proved that the metric satisfies affine invariance:

$$\delta_R\left(W^T P_1 W, W^T P_2 W\right) = \delta_R(P_1, P_2) \quad (2)$$

where W is any invertible matrix.

The Riemannian distance is the minimum length of the curve connecting two points on a Riemannian manifold [83]. It satisfies three fundamental properties of the metric space: positivity, symmetry, and triangle inequality [81]. In Fig. 1, I demonstrated the Riemannian geodesic distance between two points in the Riemannian manifold, and its correspondence to the Euclidean distance.

2.4. Tangent space

Riemannian manifold is a smooth differentiable surface, $P \in Sym+$. The linear space, which is formed by all tangent vectors at point P, is called tangent space, denoted as $Tp(\mathcal{M})$, as shown in Fig. 1. A point pi is projected to tangent space $T(\mathcal{M})$ using the logarithmic mapping $Logp(pi)$ as:

$$s_i = log_p(p_i) = p^{\frac{1}{2}} \log\left(p^{\frac{-1}{2}} p_i p^{\frac{-1}{2}}\right)^{\frac{1}{2}} \quad (3)$$

where $s_i \in \mathrm{Tp}(\mathcal{M})$, and p is the tangent point. The inverse mapping: $s_i \rightarrow p_i$, is defined by the exponential mapping $Exp_p(s_i)$:

$$p_i = Exp_p(s_i) = p^{\frac{1}{2}} \exp\left(p^{\frac{-1}{2}} p_i p^{\frac{-1}{2}}\right)^{\frac{1}{2}} \quad (4)$$

Exponential map $Exp_p(s_i) \in \mathcal{M}$ defines a unique shortest curve (geodesic) from a point p to p_i in the direction to pi in $\mathcal{M}$ so that the operation results in a point in $\mathcal{M}$ (Fig. 1). Logarithm map is an inverse of exponential map in that for $p, p_i \in \mathcal{M}$, $log p(p_i) \in T_p \mathcal{M}$ which corresponds to p_i when sent back via exponential map. Finally, geodesic distance is the length of the shortest curve that connects two points p and p_i.

2.5. Riemannian mean

Given the data $x_1, x_2, \ldots, x_{n \in} \mathcal{M}$, the Frechet mean μ_n is defined as a minimizer of the sum of the squared distances defined as follow:

$$\mu_n = argmin_{p \in \mathcal{M}} \frac{1}{n} \sum_{i=1}^{n} \rho^2(p, p_i) \quad (5)$$

where $\rho : \mathcal{M} x \mathcal{M} \rightarrow \mathbb{R}$ is a geodesic distance for $p, p_i \in \mathcal{M}$, the length of the shortest curve on manifold $\mathcal{M}$ connecting two points.

There is no closed-form expression to compute the mean. An efficient iterative algorithm to compute the Riemannian mean of SPD matrices is given in Ref. [84].

3. Methodology

3.1. Basic theory of the Riemann geometry tailored to brain networks

A subject-specific multichannel recording set $X_i \in \mathbb{R}^{SxT}$, i = 1, 2, … N_{epochs} with S and T denoting the number of EEG sensors or sources and temporal samples, respectively, is characterized by the corresponding class label $y_i \in \{1\ for\ healthy\ control, 2\ for\ SCZ\}$. The sample covariance matrix (SCM) can be estimated with Pearson's correlation coefficient (PCC), leading to a $T_s x\, S\, x\, S$ representation for every subject-specific dFCBN, where Ts denotes the number of temporal segments. The correlation-based dFCBN that describes the temporal functional dependencies between all the possible pairs of S sensors or sources is by definition an SPD matrix supported by the dimension of temporal samples T that guarantees the full rank of the derived dFCBN. The set of SPD matrices forms a cone-shaped Riemann manifold. Any operation on the SPD manifold can be better applied to the geometric structure compared to Euclidean geometry. Those SPD matrices lie on a specific Riemannian manifold denoted by Sym_S^+ which is a hypercone in an S(S + 1)/2-dimensional Euclidean space. This means that SPD matrices are associated only with positive eigenvalues. The Riemannian manifold is associated with a Euclidean tangent space at every point $P \in Sym_S^+$ [85]. The most popular metrics in the SPD geometric space are the affine-invariant Riemannian metric (AIRM) and the log-Euclidean Riemannian metric (LERM). The most famous one in brain studies and the one that will be followed here is the AIRM. This practically means that the inter-covariance distance between a pair (C_i, C_j) of SCMs (here snapshots of dFCBN) on the Riemannian manifold can be computed using the affine-invariant Riemannian metric (AIRM)-induced geodesic distance which is formulated as [86]

$$\delta(C_i, C_j) = \left\| logm\left(C_i^{-1/2} C_j C_i^{-1/2}\right) \right\|_F \quad (6)$$

with logm(.) being the log-matrix operator and.F the Frobenius norm of the matrix.

The Riemannian distance (Eq. (6)) can be employed to determine the center of mass (or geometric mean) for a given set of correlation dFCBN matrices using the Karcher/Fréchet means [82]. The whole process leads to the detection of a unique point in the Riemann manifold that satisfies the sum of squared AIRM distances for a set of SCMs described in the following equation:

$$\overline{B} = argmin_{P \in Sym_S^+} \sum_{i=1}^{N_{epochs}} \delta^2(C_i, P) \quad (7)$$

with N_{epochs} denoting the number of SCMs and δ(.,.) referring to the Riemannian distance defined in Eq. (6), while the computation of B is based on the iterative process proposed described by the following reference [86].

3.2. Riemannian alignment

The SCM representations may vary even across subjects of the same group and also across experimental time for the same subject under their placement over the Riemann manifold. Even though SCMs from the same subject can follow a similar distribution, they can be centered at a different location on the Riemann manifold. This phenomenon is called covariate shift which can destroy the performance of any classifier. Here, I adopted the methodology proposed by Ref. [87] in order to align the misplaced SCMs in the Riemann manifold. This method realigns all SCMs (data points in the manifold) around the same reference geometrical point which is the identity matrix. This procedure is described mathematically by the following equation.

$$C_i^A = \overline{B}^{-1/2} C_i \overline{B}^{-1/2} \quad (8)$$

with $\overline{B}$ being the center of mass for a set of SCMs identified by Eq. (7).

3.3. A Riemannian-based decoder for SCZ in EEG scalp recordings and virtual sensors activity

The proposed decoding scheme is called hereafter ^{R}SCZ, a framework that is built upon the Riemannian geometry concept with the main aim of introducing a robust pipeline for decoding multichannel coherent activity related to SCZ. The starting point of my pipeline is the band-pass filtering of all EEG recordings in the whole set of targeted frequency bands. Then, the derived dFCBN (SCM) per frequency band and on the multiplex scenario (see Section 4.5) across subjects are formulated with the processing steps described in Section 4.3. The epoch-based FCBN derivation is followed by the SCM alignment as described in Eq. (8) and it is performed in a group fashion and the center of mass described in Eq.

(7) is also performed across the training set of dFCBN as in Ref. [79].

After the finalization of the alignment process (Fig. 2A), and the estimation of intra-class covariance matrices (Fig. 2B), a simple supervised classification algorithm is adopted. The first step of the Minimum Distance to Riemannian Mean (MDRM) classifier is to compute the average covariance matrix k for each of the k = 1, …, K classes (here K = 2) (Fig. 2B). In the second step, MDRM computes the Riemannian distance between the unknown SCM and every intra-class covariance matrix $P_{\mathscr{R}}^{(k)}$. For every new subject-specific dFCBN epoch X, this procedure amounts to estimating K intra-class covariance matrices and then computing K eigenvalue decompositions (eq. (6)). Based on Eq. (6), every new epoch-based FCBN is assigned to the class with the minimum Riemannian distance to the Riemannian mean (Fig. 2B and C). The classification accuracy is estimated by counting the number of corrected classified epochs versus the total number of epochs. The algorithmic steps of MDRM are described below.

Algorithm. Algorithmic steps of the classification scheme based on MDRM.

Input: a set of epochs X_i of K different known classes {1 or 2}.
Input: X is an unseen subject-specific EEG epoch of an unknown class
Input: $J^{(k)}$ the set of indices of the epochs corresponding to the k-th class {1 or 2}.
Output: $\widehat{k}$ the estimated class of the test epoch corresponding to the test epoch X corresponding to the target test subject
1.Compute SCMs (dFCBNs) of X_i to obtain P_i,
2.Compute SCMs (dFCBNs) of X to obtain P,
3.for k = 1 to K do
4. $P_{\mathscr{R}}^{(k)} = \mathscr{R}\left(P_i, i \in J^{(k)}\right)$, get the Riemannian mean across train subjects and epochs (eq. (2))
5. end for
6. $\widehat{k} = argmin_k\ \delta_{\mathbb{R}}\left(P, P_{\mathscr{R}}^{(k)}\right)$ (eq. (7)), Riemannian distance between the Riemannian mean across train epochs and the target epoch
7. return $\widehat{k}$ (epoch label)

Classification on Epoch level:The decoding scheme is computed

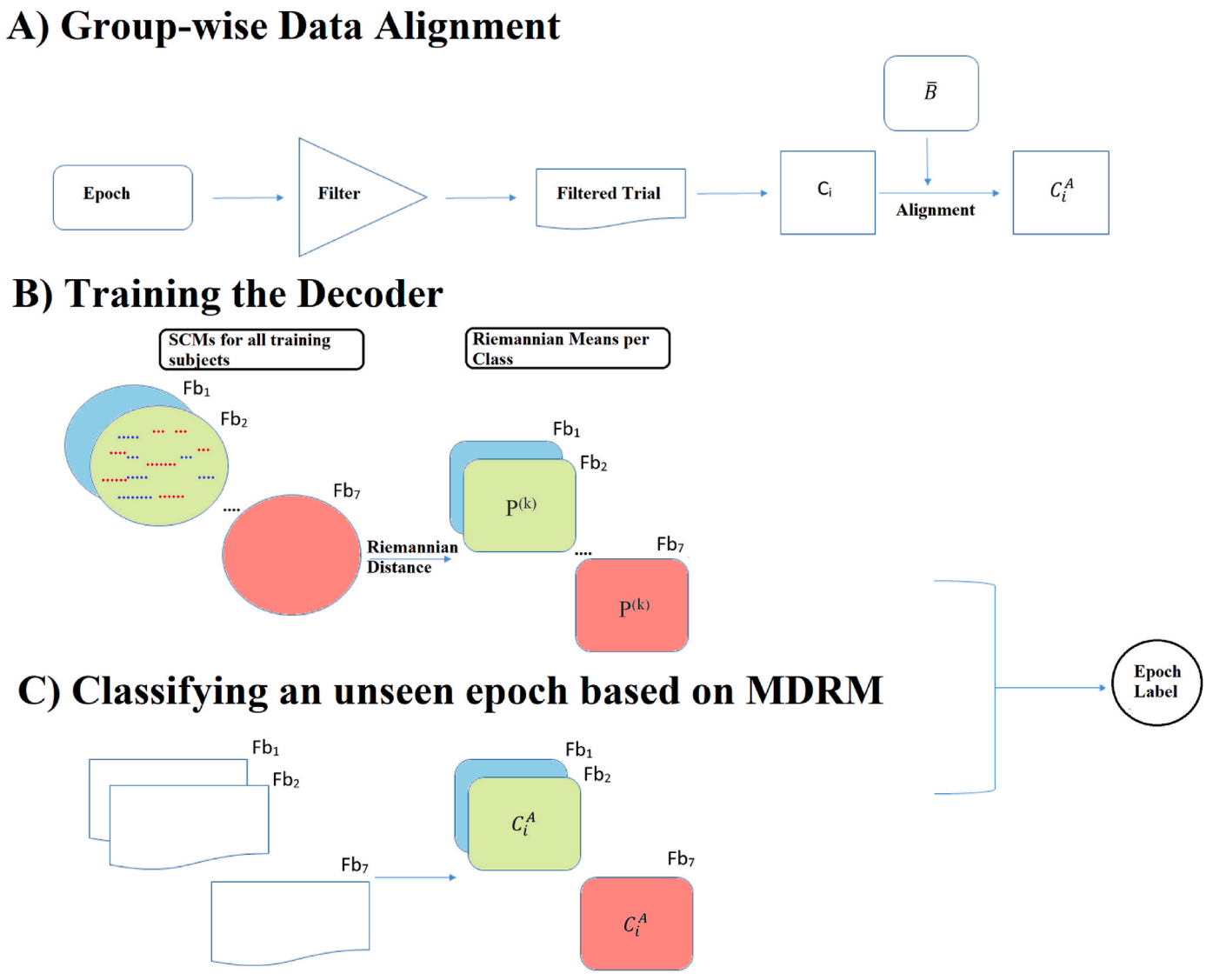

Fig. 2. Flowchart of the $^{\mathscr{R}}$SCZ framework
A. Every epoch of 2 s duration is bandpass filtered, and than a dFCBN is constructed based on a connectivity estimator which is either PCC for frequency-dependent dFCBNs or DC for the multiplex scenario, and the construction of a single dFCBN. The last process in the flowchart visualizes the realignment of all SCMs (data points in the manifold) around the same reference geometrical point which is the identity matrix as described in eq. (8) in section 3.2
B. The flowchart describes the training of the proposed decoder with the dFCBNs of the N-1 subjects, where the Riemannian mean will be estimated according to eq. (5) described in section 2.5. This process is described in the MDRM algorithm in section 3.3.
C. The dFCBN of the N^{th} subject within the LOSO-CV will be used for the testing. This process is described in the MDRM algorithm in section 3.3. From this process, the epoch label will be untangled {1 for HC, 2 for SCZ}.

across the frequency bands (see Sect. 4.6) in an ensemble way by counting the accuracy of their combination per epoch in every subject. In simple words, I adopted the majority vote rule across the seven frequency bands summing the output of the MDRM classifier on the healthy control group, and the SCZ group. I assigned the class label per epoch to one of the two classes if the label converged to the same class on at least four out of seven frequency bands. For example, if the MDRM classified an epoch as healthy control for δ, θ, α_1, α_2 brain frequencies and as SCZ for β_1, β_2, and γ brain frequencies, than this epoch will be assigned the label 1, which referred to the healthy control group. This type of classification was employed only on the frequency-dependent approach, since the multiplex scenario involved the construction of a single dFCBN.

Classification on Dynamic dimension, and subject level: I followed a dynamic functional connectivity analysis adopting a sliding-window approach of 30 non-overlapping temporal segments of 2 s duration across the first minute of resting-state recordings (see section 4.5). I measured the accuracy, sensitivity, and specificity of the correctly classified epochs over a total of 30 temporal segments. The final assigned label per subject's recording was defined by a consistent classification of at least 27 out of 30 epochs (>90 %). In the frequency-dependent scenario, I estimated the classification performance over a vector of size 1x30, which is the dynamic assignment of the epochs to the class labels after combining the frequency-dependent dFCBN per epoch. In the multiplex scenario, I adopted the aforementioned approach of assigning a label to the unique multiplex dFCBN based on the consistent classification of at least 27 out of 30 epochs.

The whole analytic plan will underline the effectiveness of the proposed ^{R}SCZ decoder in every frequency band vs the multiplexity approach and also how the performance is affected by analyzing coordinated activity in sensor and source space. In addition, MDRM and Riemannian space should be compared with a trivial classifier that manipulates functional connectivity graphs as 2D tensors (see section 3.4). A proper classifier that treats functional connectivity graphs as 2D tensors is described in the following section. In section 4.6, I described the classification performance of the ensemble and multiplex scenario.

3.4. Tensorial treatment of dFCBN

Every FBN can be straightforward represented as a second order tensor. A FBN is a 2D matrix, which is constituted by important features that reflect ordered associations between brain areas. These ordered associations could be preserved also in a low dimensional representation. To summarize, I treated FBNs as 2D tensors, and employ an algorithm called tensor subspace analysis (TSA) [88] as a suitable and convenient feature extraction strategy in this research study. TSA is a standard pattern recognition algorithm of represented the FBN as a reduced tensor. The scheme for comparison with the Riemannian geometry incorporates the k-nearest-neighbors (k-NN) algorithm, and employs the Frobenius norm as the distance metric for estimating the matching between the test FBN against the number of trained FBNs with known label.

In my previous study, I adopted TSA analysis in a multi-level cognitive arithmetic task of an increased difficult level demonstrating the importance of both tabular manipulation of FBNs, and also of the cross-frequency phase interactions within and between Frontal$^{\theta}$ and Parieto-Occipital$^{\alpha 2}$ [87]. For further details, an interested reader should see the original article presenting TSA [88], and my previous work [87]. In section 4.6, I described the classification performance of the ensemble and multiplex scenario.

4. Experimental data and preprocessing

To validate the proposed ^{R}SCZ decoding scheme, I adopted two open EEG datasets including a healthy control group and an SCZ group. In both datasets, the subjects were recorded during a resting-state eyes-closed condition.

4.1. Dataset 1

The first EEG dataset is described in every detail in the following article [37]. The study protocol was approved by the Ethics Committee of the Institute of Psychiatry and Neurology in Warsaw. All participants received a written description of the protocol and provided written consent to take part in this study. Brain activity was recorded from 14 patients diagnosed with SCZ and from 14 healthy control subjects. The SCZ group involved seven males (27.9 ± 3.3 years) and seven females (28.3 ± 4.1 years) who were diagnosed with paranoid schizophrenia according to the International Classification of Diseases (ICD)-10-CM criteria F20.0. Both groups were matched by age and gender. Brain activity was recorded with 19 EEG channels according to the International 10/20 EEG system with a sampling frequency of 250 Hz for 15 min each during an eyes-closed resting state condition. EEG time series were re-referenced to the average reference electrode before preprocessing steps.

4.2. Dataset 2

The second dataset is obtained from a public database (http://protein.bio.msu.ru/~akula/korsak/Korsak-eng.htm.). Experts from the National Centre of Mental Health of the Russian Academy of Medical Sciences Clinical provided the evaluation of these adolescents with disorders. They were diagnosed according to ICD–10 in Mental Health Research Center, Moscow and it originally included 125 boys 8–15 years old. The diagnosis was schizophrenia, childish type (F20), schizotypal disorder (F21), and schizoaffective disorder (F25) [38].

The subjects were adolescents who had been screened by psychiatrists and divided into a healthy group (n = 39) and a group with symptoms of schizophrenia (n = 45). Both groups included only two groups of Russian (Moscow) school children boys aged 10–14 years. The age of the group with schizophrenia spectrum disorders (SSDs) (schizophrenia (childhood-onset), schizotypic disorder, or schizoaffective psychosis) with comparatively homogeneous symptoms ranged from 10 years to 8 months to 14 years (12.3 ± 1.2 years). SSD group is recorded even before the pharmacological treatment appointments while subjects have been selected with the same severity.

The healthy control group included 39 healthy schoolboys aged from 11 years to 13 years and 9 months. The mean age of the healthy control group was (12.3 ± 1.3 years). Both groups were age-matched. For further details see the original article [38]. Brain activity was recorded with 16 EEG channels according to the International 10/20 EEG system with a sampling frequency of 128 Hz for 1 min each during an eyes-closed resting state condition. EEG time series were re-referenced to the average reference electrode before preprocessing steps.

4.3. Preprocessing

In both datasets, I first removed line noise using a notch filter at 50 Hz. I adopted the same denoising procedure in both datasets as I performed in the second dataset in a previous publication [89]. The algorithmic pipeline includes the combination of the well-known independent component analysis (ICA) and wavelet decomposition. Here, I used the extended Infomax algorithm implemented in EEGLAB [90]. The outcome of this procedure is 19 and 16 independent components for every subject in Dataset 1 and 2, correspondingly. Every independent component (IC) has a characteristic topography and time course. The time course of each IC was decomposed with Daubechies wavelet filters. Wavelet decomposition of IC broadband activity has been realized in 60 temporal segments of 1-sec duration for 1 min of the recordings in both datasets. Then, every wavelet subcomponent of an IC is classified as an artifact that could be ocular, muscle, or cardiac

artifacts or real brain activity based on visual inspection and with the support of kurtosis, skewness, and entropy measures [89]. For every 1-sec segment, I zeroed the artifactual wavelet segments, and I reconstructed the cleaned 1-sec IC. Then, cleaned IC time courses were recomposed from their cleaned wavelet subcomponents per temporal segment, and cleaned wavelet-ICA EEG activity was further composed of the cleaned IC time courses. In my study, the total number of wavelet subcomponents was not totally rejected in any temporal segment across IC and subjects. Power spectrum analysis was followed per subject before and after the correction procedure leading to more pronounced characteristic frequency peaks. The wavelet + ICA method has the advantage of correcting artifactual IC across the time course compared to zeroing the whole IC which leads to zeroing even true brain activity.

4.4. Source localization of resting-state activity

In my study, I employed an average head model from the reconstruction of 152 normal MRI scans (MNI template http://www.loni.ucla.edu/ICBM/) [91,92]. Four compartments of the head model named scalp, outer skull, inner skull, and cortex were extracted using the Boundary Element Method (BEM). BEM as implemented in the Brainstorm toolbox [93]. Virtual sources have been obtained from the EEG recordings via sLORETA available in Brainstorm [93]. The core of sLORETA approach is a model of linear distributed sources that solve the inverse solution problem via maximization of the correlation of neighboring sources where nearby neuronal assemblies are synchronized [94]. In addition, sLORETA minimizes the errors of the estimated virtual source activity by applying physiological constraints on the solution. sLORETA provides a high number of virtual source time series that in my study were projected in the Desikan-Killiany atlas of 68 ROIs (34 ROIs per hemisphere) [95].

4.5. Construction of dynamic functional connectivity brain network (dFCBN) in sensor and source space

EEG scalp time series and virtual source time series of both datasets were bandpass filtered with a zero-phase 3rd Butterworth filter using the *filtfilt* MATLAB function. The range of the frequency bands is the following: δ (1–4 Hz), θ (5–8 Hz), α_1 (8–10 Hz), α_2(10–13 Hz), β_1(14–20 Hz), β_2(21–30 Hz), and low-γ (31–45 Hz). In my study, I estimated dFCBN in both sensor and source space, and for every frequency band independently and under the novel proposed multiplex approach. In the frequency-dependent scenario, I adopted the Pearson correlation coefficient (PCC) applied on the Hilbert envelope of the bandpass filtered pairs of sensor or ROI-based time series (Fig. 3). In the proposed multiplex scenario, I combined the set of the Hilbert envelope of the bandpass filtered time series per sensor and ROI (virtual sources) to estimate the multiplex interaction for every pair of sensors or ROI-based time series. For that purpose, I adopted the distance correlation metric (DC) (see Fig. 3, and in Ref. [96] for application in functional magnetic resonance imaging - fMRI). The estimation of functional coupling strength in every frequency band and in the multiplex approach is shown in Fig. 3 for a pair of EEG sensors. In my dynamic analysis, I constructed a snapshot of dFCBN for every 2 s of recordings with no overlapping up to the 1 min of recordings. This process produces 30 snapshots for every subject-specific constructed dFCBN in both frequency-dependent and multiplex approaches and in both sensor and source space (Fig. 4). In the frequency-dependent scenario, I constructed seven dFCBNs, one per frequency band, and a single multiplex dFCBN per subject. Both PCC, and DC take value within [0,1], since I kept the absolute values of PCC.

On the virtual source space, the aforementioned analysis was performed on both the whole source space of 68 ROIs, and on the target DMN, focusing on twelve ROIs, six for the anterior-DMN (a-DMN), and six for the posterior-DMN (*p*-DMN). Every snapshot of the dFCBN, is a functional connectivity network of dimension [68 x 68] on the whole source space, and [12 x 12] on the DMN subnetwork space that tabulates the functional coupling strength between every pair of sources. Similarly, every snapshot of dFCBN on the sensor level is of dimension {EEG sensors} x {EEG sensors} (19 x 19, and 16 x 16 in datasets).

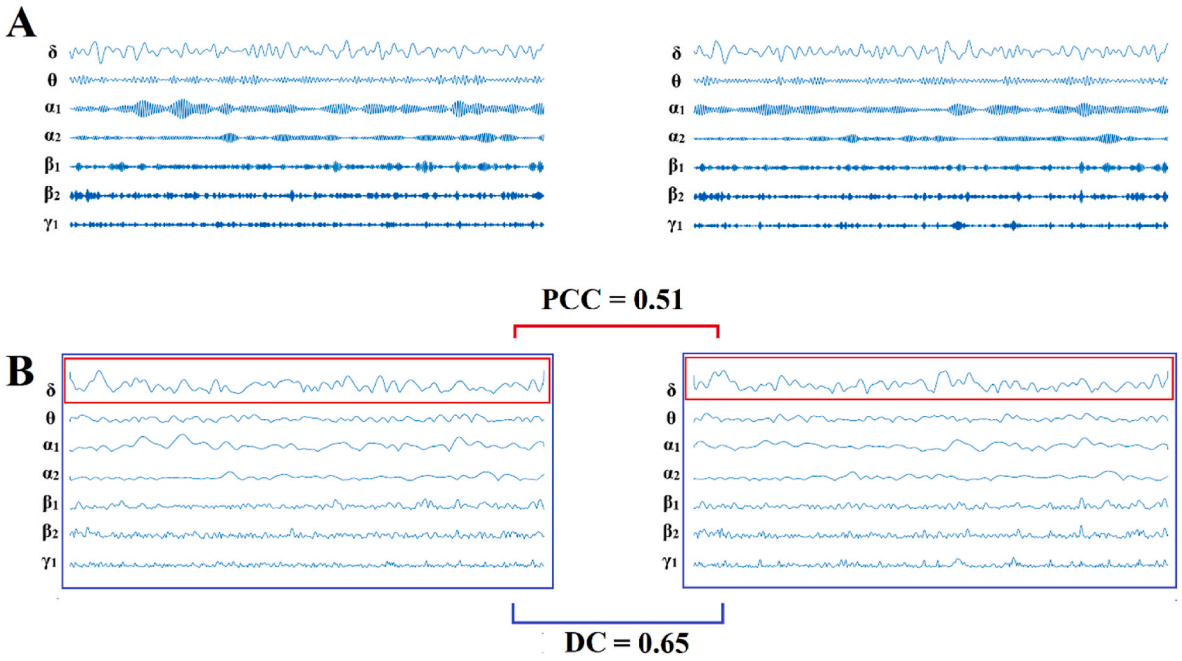

Fig. 3. Demonstration of correlation of the envelope of two bandpass filtered time series vs the proposed multiplex scenario between two sets of bandpass filtered time series over frequency bands δ to low-γ. A. Two sets of bandpass filtered time series extracted from FP1 and FP2 sensors from the first control subject of dataset 1. B. The Hilbert envelope of the two sets of bandpass filtered time series presented in A. I demonstrated the PCC applied on δ bandpass filtered time series and the DC applied over the two sets of seven bandpass filtered time series.

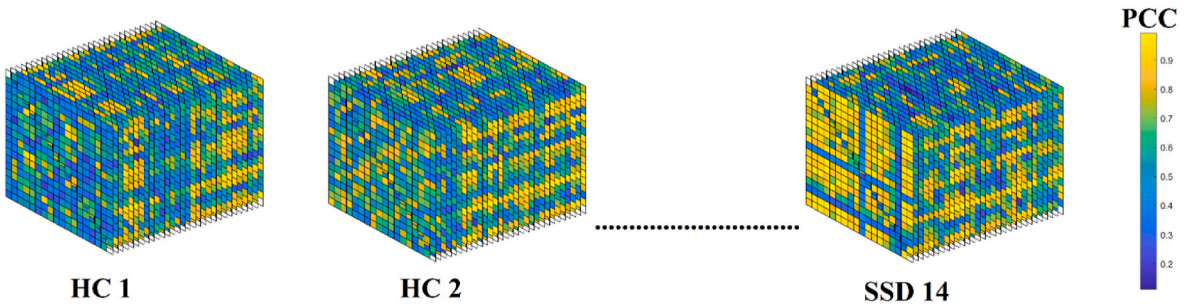

Fig. 4. (Dataset 1) Construction of individualized dFCBN from the multichannel EEG sensor recordings that were bandpass filtered in the δ frequency band with the use of PCC as connectivity estimator.

4.6. Classification performance of the ensemble and multiplex scenario

I adopted a leave-one-out subject cross-validation scheme (LOSO-CV) where the classification encoding procedure under the Riemannian space was realized on the dFCBN of the N-1 subjects ((N-1) x 30 temporal segments) and the decoding procedure on the target subject-specific dFCBN (30 temporal segments). A similar LOSO-CV was followed also for the tensorial treatment of the frequency-dependent, and multiplex scenario employing the combination of TSA, and k-NN. Here, I used a $k = 5$ for k-nearest neighbors in both datasets.

Classification on Epoch level: For the frequency-dependent scenario, and the epoch level, I assigned the class label per epoch to one of the two classes if the label converged to the same class on at least four out of seven frequency bands (majority vote rule). For example, if the MDRM/TSA-k-NN classified an epoch as healthy control for δ, θ, α_1, α_2 brain frequencies and as SCZ for β_1, β_2, and γ for brain frequencies, than this epoch will be assigned the label 1, which referred to the healthy control group. This type of classification was followed only to the frequency-dependent FCBNs, since in the multiplex scenario, a single dFCBN was constructed.

Classification on Dynamic dimension, and subject level: I followed a dynamic functional connectivity analysis adopting a sliding-window approach of 30 non-overlapping temporal segments of 2 s duration across the first minute of resting-state recordings (see section 4.5). I measured the accuracy, sensitivity, and specificity of the correctly classified epochs over a total of 30 temporal segments. The ensemble strategy of the frequency-dependent dFCBN led to a vector of size 1 x 30, with the relevant class labels {1 or 2}. For the frequency-dependent dFCBN, the final assigned label per subject's recording was defined by a consistent classification of at least 27 out of 30 epochs (>90 %). Similarly, for the multiplex scenario, I assigned a label per subject's recording which is supported by a consistent classification of at least 27 out of 30 epochs (>90 %). The whole analysis was followed independently in both datasets, sensor, whole source level, and DMN, and classification approach (Riemannian vs tensorial space).

Whole source space: On the whole virtual source level, I followed a similar classification approach adopting LOSO-CV focusing on dFCBN tailored to the 68 ROIs. The produced FBN were of size {virtual sources x virtual sources}, which practically means of size [68 x 68].

DMN: On the virtual source level, I followed a similar classification approach adopting LOSO-CV focusing on dFCBN tailored to DMN. The produced FBN were of size {virtual sources x virtual sources}, which practically means of size [12 x 12].

I compared the performance metrics between ensemble vs multiplex approaches, and MDRM vs TSA-k-NN classification schemes. See the Statistics section.

4.7. Statistics

To support the superiority of the proposed ^{R}SCZ framework in combination with the multiplex scenario and DC metric, I applied a Wilcoxon Rank-Sum test on the accuracy, sensitivity, and specificity obtained from the PCC and the ensemble scenario vs the DC and the multiplex scenario. This statistical analysis was followed in both datasets comparing the performance metrics between ensemble, and DC/multiplex scenario independently in sensor and source space. This statistical analysis was repeated independently for the Riemannian geometry, and the TSA-k-NN.

I also applied a Wilcoxon Rank-Sum test on the accuracy, sensitivity, and specificity between Riemannian geometry, and TSA-k-NN on the ensemble – multiplex scenarios, on the DMN level.

Finally, I applied a Wilcoxon Rank-Sum test to compare group-averaged and DMN network averaged DC strength within and between the DMN brain areas across the four groups in both datasets. The p-values were Bonferroni corrected.

5. Results

I reported the findings independently for sensor and source space in both datasets while I demonstrated representative FCBN for both groups and both datasets targeting on the default mode network (DMN) brain areas.

5.1. Performance of ^{R}SCZ framework in EEG sensor and whole virtual space

The multiplex scenario outperformed the ensemble approach in both datasets, in both sensor, and source space, and following both the proposed MDRM Riemannian decoding approach, and the comparable TSA-k-NN classification scheme (Tables 1 and 2).

Riemannian geometry, and MDRM: The performance of the proposed ^{R}SCZ in the EEG sensor space and in the multiplex scenario was **82.14** for the first dataset and **85.71** for the second compared to the ensemble strategy of **78.50** and **72.62**, correspondingly. The performance of my ^{R}SCZ in the whole virtual space and in the multiplex scenario was **92.85** for the first dataset, and **100** for the second compared to the ensemble strategy of **85.71** and **89.29** performance, correspondingly (Tables 1A and 2A).

TSA and k-NN scheme: The performance of the TSA-k-NN classification scheme in the EEG sensor space and in the multiplex scenario was **82.14** for the first dataset and **76.19** for the second compared to the ensemble strategy of **75** and **69.05**, correspondingly. The performance of my ^{R}SCZ in the whole virtual space and in the multiplex scenario was **85.71** for the first dataset, and **79.76** for the second compared to the ensemble strategy of **82.14** and **77.38** performance, correspondingly (Tables 1B and 2B).

The performance of Riemannian geometry was higher compared to TSA-k-NN classification scheme in any dimension of the present exploratory framework (sensor, and source level, ensemble – multiplex approach), and in both datasets. Additionally, the performance on the virtual space was higher compared to the sensor space in the ensemble, and multiplex approaches, and in both datasets.

Table 1

A. Classification Performance of ^{R}SCZ framework in the sensor and whole virtual space, and in the ensemble and multiplex approaches for Dataset 1 based on **MDRM.** I reported the accuracy, sensitivity, and performance based on the corrected temporal segments while the performance corresponds to the correct classified sample based on the adopted threshold of at least 27 correct classified epochs out of the total 30 temporal segments.

	Sensor Space			Virtual Space		
	PCC/Ensemble	DC/Multiplex	Statistics	PCC/Ensemble	DC/Multiplex	Statistics
Accuracy	84.14 ± 3.11	94.38 ± 3.85	$p = 4.5x10^{-11}$	86.54 ± 6.72	97.56 ± 3.05	$p = 6.3x10^{-12}$
Sensitivity	83.09 ± 4.32	93.43 ± 2.71	$p = 3.6x10^{-11}$	85.16 ± 5.22	96.82 ± 2.93	$p = 5.4x10^{-12}$
Specificity	81.45 ± 4.11	92.43 ± 3.69	$p = 3.9x10^{-11}$	84.94 ± 5.72	95.65 ± 3.83	$p = 9.2x10^{-13}$
Performance	**78.50**	**82.14**		**85.71**	**92.85**	

B. Classification Performance of ^{R}SCZ framework in the sensor and whole virtual space, and in the ensemble and multiplex approaches for **Dataset 1** based on **TSA-k-NN scheme**. I reported the accuracy, sensitivity, and performance based on the corrected temporal segments while the performance corresponds to the correct classified sample based on the adopted threshold of at least 27 correct classified epochs out of the total 30 temporal segments.

	Sensor Space			Virtual Space		
	PCC/Ensemble	DC/Multiplex	Statistics	PCC/Ensemble	DC/Multiplex	Statistics
Accuracy	72.31 ± 3.67	81.72 ± 3.09	$p = 6.7x10^{-11}$	77.12 ± 2.78	86.34 ± 3.78	$p = 5.4x10^{-11}$
Sensitivity	73.45 ± 4.11	82.62 ± 2.98	$p = 4.5x10^{-12}$	76.86 ± 3.71	87.42 ± 3.69	$p = 4.7x10^{-12}$
Specificity	71.85 ± 2.93	92.43 ± 3.69	$p = 3.9x10^{-11}$	84.94 ± 5.72	87.44 ± 3.18	$p = 9.2x10^{-13}$
Performance	**75**	**82.14**		**82.14**	**85.71**	

Table 2

A. Classification Performance of ^{R}SCZ framework in the sensor and whole virtual space, and in the ensemble and multiplex approaches for Dataset 2 based on **MDRM**. I reported the accuracy, sensitivity, and performance based on the corrected temporal segments while the performance corresponds to the correct classified sample based on the adopted threshold of at least 27 correct classified epochs out of the total 30 temporal segments.

	Sensor Space			Virtual Space		
	PCC/Ensemble	DC/Multiplex	Statistics	PCC/Ensemble	DC/Multiplex	Statistics
Accuracy	74.32 ± 6.25	88.61 ± 3.74	$p = 8.1x10^{-10}$	89.68 ± 5.42	98.42 ± 3.82	$p = 5.2x10^{-12}$
Sensitivity	72.26 ± 5.82	86.84 ± 3.97	$p = 7.3x10^{-11}$	88.68 ± 4.88	97.48 ± 3.14	$p = 4.5x10^{-11}$
Specificity	71.53 ± 5.92	85.09 ± 3.51	$p = 6.2x10^{-12}$	87.79 ± 5.32	96.48 ± 3.32	$p = 6.7x10^{-12}$
Performance	72.62	85.71		**89.29**	**100**	

B. Classification Performance of ^{R}SCZ framework in the sensor and whole virtual space, and in the ensemble and multiplex approaches for Dataset 2 based on **TSA - k-NN scheme.** I reported the accuracy, sensitivity, and performance based on the corrected temporal segments while the performance corresponds to the correct classified sample based on the adopted threshold of at least 27 correct classified epochs out of the total 30 temporal segments.

	Sensor Space			Virtual Space		
	PCC/Ensemble	DC/Multiplex	Statistics	PCC/Ensemble	DC/Multiplex	Statistics
Accuracy	68.23 ± 3.22	77.34 ± 3.92	$p = 7.6x10^{-11}$	79.17 ± 4.32	78.12 ± 3.42	$p = 5.7x10^{-11}$
Sensitivity	67.72 ± 3.92	78.54 ± 3.25	$p = 6.4x10^{-11}$	78.76 ± 4.09	79.17 ± 3.54	$p = 4.1x10^{-12}$
Specificity	68.33 ± 4.12	76.79 ± 3.42	$p = 6.0x10^{-11}$	77.18 ± 3.92	77.51 ± 3.42	$p = 5.2x10^{-11}$
Performance	**69.05**	**76.19**		**77.38**	**79.76**	

5.2. Performance of ^{R}SCZ framework in EEG DMN virtual space

Following the same cross-validation approach on the DMN virtual space, I untangled that the multiplex scenario outperformed the ensemble approach in both datasets, and in both the proposed MDRM Riemannian decoding approach, and the comparable TSA-k-NN classification scheme (Tables 3 and 4). The Riemannian geometry manipulation of multiplex subject-specific dFCBN anatomical restricted on the DMN subnetwork succeeded an absolute performance (100) in both datasets. The TSA with the incorporation of k-NN classifier performed also well in both datasets, and the multiplex scenario reaching the 85.71, and 88.1, in dataset 1 and 2, correspondingly.

5.3. Aberrant DMN topologies in SCZ and in SSD

In the present study, I parcellated the virtual source space into 68 brain areas according to the Desikan-Killiany cortical atlas partitions [97]. I decided to demonstrate the group-averaged FBN between the DMN in both datasets as a target brain area at resting-state for major psychiatric disorders [79]. From a total of 68 brain areas, I focused on 12 bilateral cortical DMN brain regions including lateral orbitofrontal, medial orbitofrontal, rostral anterior cingulate, parahippocampal, isthmus cingulate, posterior cingulate, and precuneus. The DMN regions were further grouped into the anterior and posterior DMN in order to understand how the DC is altered within and between those two groups

Table 3

Classification Performance of ^{R}SCZ framework in the DMN virtual space, and in the ensemble and multiplex approaches for Dataset 1 based on MDRM, and TSA-kNN classification schemes. I reported the accuracy, sensitivity, and performance based on the corrected temporal segments while the performance corresponds to the correct classified sample based on the adopted threshold of at least 27 correct classified epochs out of the total 30 temporal segments.

	MDRM			TSA-kNN		
	PCC/Ensemble	DC/Multiplex	Statistics	PCC/Ensemble	DC/Multiplex	Statistics
Accuracy	75.32 ± 3.41	98.76 ± 1.61	$p = 8.9x10^{-11}$	65.24 ± 3.91	83.61 ± 3.11	$p = 6.1x10^{-12}$
Sensitivity	74.65 ± 3.82	98.74 ± 1.72	$p = 5.7x10^{-11}$	64.51 ± 3.28	84.57 ± 3.92	$p = 4.9x10^{-13}$
Specificity	75.17 ± 4.09	99.18 ± 1.06	$p = 6.9x10^{-11}$	65.29 ± 3.37	83.78 ± 3.81	$p = 7.3x10^{-12}$
Performance	**71.42**	**100**		**67.85**	**85.71**	

Table 4
Classification Performance of ^{R}SCZ framework in the DMN virtual space, and in the ensemble and multiplex approaches for Dataset 2 based on MDRM, and TSA-kNN classification schemes. I reported the accuracy, sensitivity, and performance based on the corrected temporal segments while the performance corresponds to the correct classified sample based on the adopted threshold of at least 27 correct classified epochs out of the total 30 temporal segments.

	MDRM			TSA-kNN		
	PCC/Ensemble	DC/Multiplex	Statistics	PCC/Ensemble	DC/Multiplex	Statistics
Accuracy	84.26 ± 3.08	99.02 ± 1.03	$p = 6.1x10^{-12}$	76.72 ± 3.18	89.61 ± 4.15	$p = 3.2x10^{-12}$
Sensitivity	85.36 ± 3.71	98.91 ± 1.12	$p = 4.8x10^{-13}$	75.82 ± 3.73	88.42 ± 4.32	$p = 7.4x10^{-13}$
Specificity	84.48 ± 4.18	99.23 ± 1.09	$p = 5.6x10^{-12}$	77.41 ± 3.82	89.65 ± 4.65	$p = 7.9x10^{-13}$
Performance	**83.33**	**100**		**67.85**	**88.1**	

in the target groups. The anterior part of the DMN includes left and right lateral orbitofrontal, medial orbitofrontal, and rostral anterior cingulate regions, and the posterior DMN consists of the left and right isthmus cingulate, posterior cingulate, and precuneus regions.

I first averaged the DC multiplex subnetworks across the 30 temporal segments at the subject level and secondly across the subjects per group. Fig. 5A illustrates the group-averaged DC multiplex DMN network topologies for both datasets and groups. Fig. 5B demonstrates the mean and standard deviation of DC functional strength for the intra-anterior DMN brain areas, the intra-posterior DMN brain areas, and the inter anterior-posterior DMN brain interactions for both datasets and groups. Interestingly, I detected significant group differences in both datasets and in both anterior and posterior parts of the DMN with higher group mean DC values for the target groups compared to the HC group (Fig. 5B). On the opposite, the HC groups showed significant higher DC values in the inter anterior-posterior DMN interactions compared to the target groups in both datasets. Additionally, significantly higher values were detected for the HC adult and SCZ groups of Dataset 1 compared to the homolog groups of Dataset 2. This observation of higher multiplex DC functional strength in the mature older HC group compared to the adolescents justified a sensitive of this index to the maturation of the DMN. The p-values related to the group comparisons shown in Fig. 5B are reported in the caption of Fig. 5. All the comparisons were significant ($p < 0.05$) passing the Bonferroni correction ($p' < p/8$).

6. Discussion

6.1. Summary of findings

In this study, I presented a novel decoding scheme for the detection of SCZ based on the Riemannian geometry called $^{\mathcal{R}}$**SCZ** decoder. My analytic pipeline explored the SCM representations of frequency-dependent EEG signals in an ensemble way based on the PCC estimator and also under a multiplex scenario based on the DC metric. I adopted MDRM as a proper classifier for the Riemannian approach, and TSA representation of dFCBNs with the incorporation of k-NN classifier for comparative purpose of the proposed analytic scheme. I demonstrated the performance of $^{\mathcal{R}}$**SCZ** decoder for the very first time in the literature in two open EEG datasets, and in both sensor and source space. The classification results supported the proposed $^{\mathcal{R}}$**SCZ** decoding scheme of companying DC as a multiplex index encountering the coupling between two brain areas by incorporating the whole set of frequency-dependent time-series (PCC vs DC), and the representations of dFCBNs on the SPD manifold performing the classification on the geometric structure rather than the Euclidean geometry (MDRM vs TSA-k-NN). The classification performance was consistent higher in both datasets for the proposed $^{\mathcal{R}}$**SCZ** decoding scheme of integrating DC and Riemannian geometry compared to PCC-TSA-k-NN in both sensor, and source space. However, the performance was improved on the source level in both decoding schemes. The performance of $^{\mathcal{R}}$SCZ decoder was 92.85 for the first dataset, and 100 for the second dataset on the whole virtual source space focusing on the 68 ROIs, and 100 in both datasets focusing on the DMN subnetwork. Based on my findings presented here, I recommend the $^{\mathcal{R}}$**SCZ** decoder with DC metric as a proper analytic framework that takes the advantage of the multiplex interactions between brain areas even at resting-state, and the manipulation of dFCBNs as a collection of SPD matrices forming a cone-shape Riemannian manifold.

6.2. Riemannian manifold, and SPD matrices

Functional connectivity brain networks are formed with connectivity estimators like the covariance and Pearson's correlation forming SPD matrices. A collection of SPD matrices forms a Riemannian manifold, where the operations on this manifold can be performed better on the

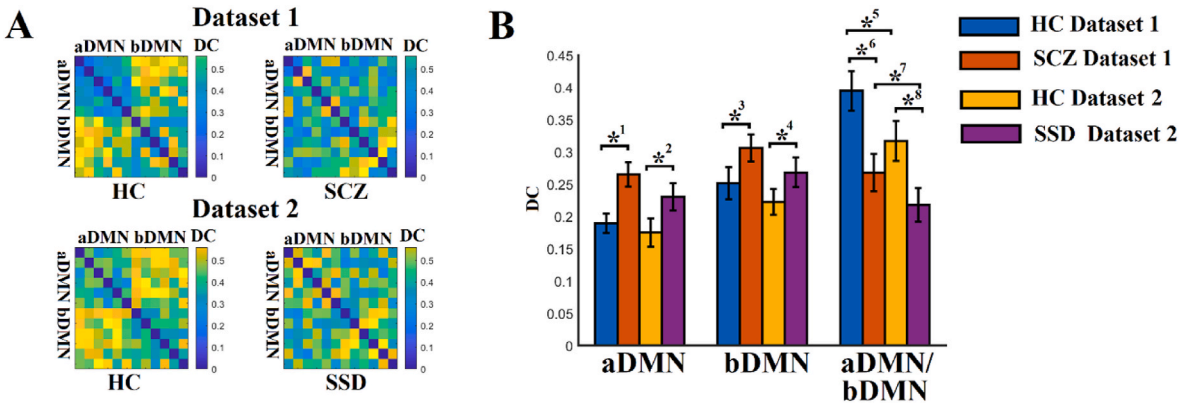

Fig. 5. Group-averaged DC multiplex DMN network topologies A.Group-averaged multiplex DMN network topologies for both datasets and groups.B. The mean and standard deviation of DC functional strength for the intra-anterior DMN brain areas, the intra-posterior DMN brain areas, and the inter anterior-posterior DMN brain interactions for both datasets and groups **(aDMN - anterior part of the Default Mode Network; bDMN - posterior part of the Default Mode Network)**.
(Related p-values linked to comparison pairs as shown in Fig. 5B:
$p_1 = 6.7 \times 10^{-12}$, $p_2 = 4.3 \times 10^{-9}$, $p_3 = 8.1 \times 10^{-5}$, $p_4 = 7.8 \times 10^{-5}$
$p_5 = 4.9 \times 10^{-8}$, $p_6 = 5.4 \times 10^{-13}$, $p_7 = 1.3 \times 10^{-4}$, $p_8 = 5.9 \times 10^{-5}$).

relevant geometric structure compared to the Euclidean geometry. However, the geometric properties of SPD manifold have not yet fully adopted by the neuroimaging community on a very large number of brain connectivity research studies. Only a small number of connectivity studies have been conducted on the SPD matrices' space. Just to name a few, Varoquaux et al. [74], and Yamin et al. [98], applied Riemannian geometry to evaluate group-averaged covariance matrices, Ginestet et al. [99], and Varoquaux et al. [74], employed geodesic distance for statistical testing, Rahim et al. [75], estimated individual covariance matrix on a Riemannian manifold, Davoudi et al. [100], and Xie et al. [101], presented a dimensionality reduction Riemannian-based technique for machine learning, Riemannian geometry has been applied to the coordination of multiple brain areas [77,70], while Riemann approach has not yet extensively been investigated in the context of clinical neuroscience, and especially in psychiatry [71].

6.3. Applications of Riemann geometry

Even though the Riemann geometry has not be extensively employed on connectivity neuroimaging studies with major neuroimaging modalities (MEG/diffusion MRI/MEG/fMRI), its benefits were well explored on brain-computer interface (BCI) EEG paradigms. These methods have been investigated in the last decade mainly in the brain-computer interface (BCI) society [72,73,77,70,102–106] with the geometric manipulations of SCM representations of functional connectivity graphs enriching our understanding about brain functionality. Last years, the Riemannian geometry of SPD matrices received much attention in the neuroscience community due to its effectiveness to deal with the main problems that any researcher encounters in the design of basic signal processing pipelines like artifact contamination, the variability across subjects and sessions, non-stationarity of the brain signal, inter-site variability, etc [72,107,108]. Riemannian geometry-based features representation extracted from multichannel EEG recordings has shown consistent and high-performance classification schemes in many classification problems [79,106,109,110]. Despite its revisiting popularity [72], Riemannian approaches have not been fully explored in clinical neurophysiology [71] and especially in SCZ.

6.4. Functional connectivity at resting-state, and the DMN

Functional connectivity at resting-state refers to the temporal associations of spontaneous brain activity among spatially distinct brain areas [111]. The derived functional connectivity patterns, namely the resting-state networks (RSNs), characterize the individual differences in intrinsic brain functionality [112]. Recent neuroimaging studies investigated spectrum, and connectivity-based features extracted from resting-state condition (eyes-closed and/or eyes-opened) with the objective criterion to detect uniquely one subject versus the rest of the cohort under a brain-fingerprinting framework [113–117]. One such RSN, that was the target of many researcher studies is the DMN. The DMN is active during oriented mental activity at resting-state that includes mind wandering, self-reflection, theory of mind etc, and is suppressed in the presence of a natural or lab-oriented stimulus [118,119]. Raichle and colleagues [118] proposed the term "default-mode", while Raichle et al. [120], established the presence of DMN on resting-state fMRI (rs-fMRI) [121]. The DMN has been validated as a reproducible network at resting-state [122–124], while it has low intra, and inter-subject variability [123–125] across different data acquisition, and analytic protocols [122,126]. It was proved that the DMN has been associated with specific cognitive functions that include self-monitoring and autobiographical thoughts, predictive planning, and stimulus-independent thought [127–130].

6.5. Evidences on aberrant functional connectivity at resting-state in the DMN in SCZ patients

Targeted resting-state and DMN research studies have been performed on numerous functional modalities that include EEG/MEG/fMRI/PET [131–139]. A PET-fMRI study at resting-state revealed an association between local glucose consumption with the functional connectivity within DMN [139]. EEG reflects a direct measurement of brain electrical activity, and has been recognized as the most cost-effective noninvasive modality for the studying of resting-state activity, and connectivity patterns within DMN [132–134]. Aberrant DMN connectivity patterns have been reported in SCZ [68,136,137], and in various psychiatric disorders [69,138]. A rs-fMRI study in SCZ following an independent component analysis to extract the RSN, including the target DMN reported altered DMN connectivity. This aberrant connectivity pattern may underlie negative symptoms, delusions, and hallucinations in SCZ patients [68]. The authors reported a classification accuracy of 76.9 % to differentiate SCZ patients from age-matched healthy controls. A recent unique EEG study investigated how six major psychiatric disorders, including mild cognitive impairment, and Alzheimer's disease altered the within DMN frequency-dependent connectivity patterns across frequency bands [69]. They used a common healthy control group as a template to proceed with the adopted statistical analysis, while they employed the famous phase locking value (PLV) as a connectivity estimator. They adopted the Desikan atlas revealing aberrant connectivity patterns compared to the age-matched HC group mainly in θ and β_2 frequency bands, while their analysis didn't involve the γ frequency. The authors didn't report any classification performance of the DMN subnetwork connectivity patterns across the target groups, and the healthy control.

6.6. Novel findings on disrupted multiplex connectivity within the DMN in SCZ groups

My study involved the analysis of two open EEG SCZ datasets on both the sensor and virtual source level targeting the DMN. I followed a trivial frequency-dependent dynamic connectivity analysis using the PCC estimator compared to the proposed multiplex index adopting the DC metric. In addition, I proposed a Riemannian framework for the dFCBNs compared to a typical classification scheme working on the Euclidean geometry. My proposed ^{R}SCZ framework provides a common template for every neuroscientist working on various psychiatric disorders with EEG modality.

The proposed multiplex DC metric revealed significant findings for SCZ disorder (Fig. 5B). The multiplex DC functional strength between brain areas located on either the anterior or posterior part of the DMN showed hyperactivity for the SCZ groups compared to the HC group. On the contrary, the multiplex DC functional strength between brain areas that are located in the anterior and posterior part of DMN showed hypoactivity for the SCZ group compared to the HC group. Importantly, this hypoactivity was also observed in the homolog groups (either HC or SCZ) between the two datasets. This evidence supports further the multiplex DC metric that validates its sensitivity for the detection of SCZ and also developmental trends in both the healthy and target group.

6.7. Altered DMN multiplex connectivity in SCZ, and deficits in self-awareness

Here, I untangled a novel potential biomarker tailored to SCZ, since it is well justified the role of a disrupted DMN in the pathogenesis of SCZ, linking both disturbed DMN connectivity and activity to its psychopathology and cognitive deficits [136]. DMN connectivity is essential for self-related cognition in healthy populations, while an aberrant DMN connectivity pattern might contribute to the excessive self-awareness and cognitive rigidity often observed in SCZ [140]. Self-awareness and information processing are heavily dependent of the functional

connectivity within thalamo-limbic, and prefrontal – parietal brain areas where both networks mediate the perception of subjective – experience, and self-awareness that are disrupted by the onset of SCZ [141]. The prefrontal – parietal brain network involves the anterior-posterior part of the DMN that was first investigated here under a multiplex connectivity analysis in two different EEG-SCZ datasets. Practically, the altered DMN multiplex connectivity observed in SCZ groups compared to the HC groups is a sensitive index of the excessive self-awareness in SCZ individuals [22,24,26,111,136,140,141].

Research studies investigated the mind wandering in SCZ as it is captured at resting-state condition, and how it affected the switch between different cognitive states. They observed a loss in the DMN's ability to efficiently switch between different cognitive states, leading to a prolonged focus on internal cognition [142,143]. They also revealed a longer and frequent duration of mind-wandering episodes following a dynamic functional connectivity analysis on the DMN [144].

While DMN connectivity is essential for self-related cognition, an aberrant DMN connectivity pattern in SCZ individuals that deviates from their healthy control counterparts might contribute to the excessive self-consciousness and cognitive rigidity often observed in SCZ [142–144]. Impaired self-awareness is associated with increased working memory deficits, depression, suicidal behaviors, and increased symptom severity in SCZ patients [145]. The aberrant dynamic multiplex connectivity strength within the DMN that was revealed here is in line also with these findings, and can be seen as a DMN-based connectivity index that quantifies the deficits in self-referential processing and disturbances in self-awareness observed in SCZ.

6.8. Sensitivity of multiplex index on developmental trends

Finally, I untangled a higher multiplex functional connectivity strength between the anterior-posterior part of DMN in the mature HC of dataset 1 compared to the adolescents HC of dataset 2 supporting also a sensitive of this index to capture developmental trends of the maturation of brain networks within the DMN [146]. These findings showed that the multiplex index is sensitive to maturation of brain connectivity, a trend that should be extensively be validated in large samples.

6.9. Short summary of the important findings

The most important outcome of my ^{R}SCZ framework was the combined SCM representations across frequency bands (ensemble strategy), the validation of a novel multiplex index, and the absolute classification performance (100 %) for the detection of SCZ in two independent datasets. The absolute performance has been succeeded in virtual source space within the default mode network (DMN) with the multiplex approach. EEG signals related to the datasets were recorded with a different experimental setup which further supported my ^{R}SCZ framework.

6.10. Limitations

One of the limitations of the present study is the small number of subjects in the first dataset and also the lack of female subjects in the second dataset. Moreover, the source localization approach has been performed as a way to further validate my findings in relation to the current literature. However, the source localization has been performed with MRI templates instead of individual MRI. An extension of this study could be over the use of individual MRI for the source localization, across a larger sample, and also across several scan sites (harmonization).

EEG is the most common neuroimaging technique in clinical practice tailored to SCZ due to its low-cost, its non-invasiveness, and its embedding in wearable devices. Numerous algorithms that can be classified as artificial intelligence have been proposed so far for the automatic identification of SCZ individuals. I strongly believe that the ^{R}SCZ framework will be a valuable decoding approach for psychiatrists not only due to its high classification performance but also due to its interpretation of findings in relation to the current knowledge.

6.11. Future directions

To be pragmatic, a large EEG study is needed to collect longitudinal recordings from different psychiatric disorders across different sites. Such a study is needed in the literature for many reasons. A large sample size is important for supporting statistically powered, and reproducible results [147]. Harmonization of datasets across sites is also relevant to the reproducibility of research findings by addressing heterogeneities in multi-centric studies [148,149]. Adopting my dominant coupling modes model (DoCM) could inform us about the preferred coupling modes between virtual brain sources which can include a mixture within-frequencies, and cross-frequency couplings patterns [117]. Finally, a common pre-processing, and processing analytic plan of brain recordings across psychiatric dimensions will further enhance our understanding of aberrant connectivity patterns at resting-state and/or experimental tasks linked to these disorders compared to healthy controls.

7. Conclusions

In the present study, I designed a ^{R}SCZ framework that attempted to present a complete set of preprocessing steps in order to discriminate HC from SCZ individuals. For that purpose, I analyzed two open EEG resting-state databases that include both HC and SCZ subjects. I attempted to validate the superiority of multiplex dFCBN adopting a DC metric versus a frequency-dependent dFCBN scenario adopting PCC under both a Riemannian geometry, and a TSA-k-NN machine learning scheme. I validated the superiority of ^{R}SCZ framework with the multiplex approach in both sensor and virtual space in both datasets compared to the frequency-dependent approach. The proposed ^{R}SCZ framework with the multiplex approach performed an absolute classification performance (100 %) for the detection of SCZ in two independent datasets derived from different experimental setups on the virtual space within the DMN.

The multiplex DC index estimated the functional connectivity between virtual sources characterized the brain activity of brain areas located on the anterior-posterior part of the DMN. The DMN-based dFCBNs constructed from resting-state conditions, and the absolute performance of the ^{R}SCZ framework to discriminate SCZ from HC group underlined the sensitivity of my approach to the disrupted self-awareness of the SCZ group. This result further indicates that my ^{R}SCZ framework can provide invaluable support to psychiatrists, and clinicians in SCZ diagnosis, and prognosis.

Software

The implementation of the distance correlation metric can be found in my github repository

https://github.com/stdimitr/multiplex_functional_connectivity_distcorr/tree/main.

CRediT authorship contribution statement

Stavros I. Dimitriadis: Writing – review & editing, Writing – original draft, Software, Methodology, Investigation, Funding acquisition, Formal analysis, Data curation, Conceptualization.

Declaration of competing interest

The author declares that they have no known competing financial interests or personal relationships that could have appeared to influence the work reported in this paper.

Acknowledgment

SID is supported by a Beatriu de Pinós fellowship (2020 BP 00116).

Appendix A. Supplementary data

Supplementary data to this article can be found online at https://doi.org/10.1016/j.compbiomed.2024.108862.

References

[1] P.D. Harvey, M. Strassnig, Predicting the severity of everyday functional disability in people with schizophrenia: cognitive deficits, functional capacity, symptoms, and health status, World Psychiatr. 11 (2) (Jun. 2012) 73–79, https://doi.org/10.1016/j.wpsyc.2012.05.004.

[2] K. Kaneko, Negative symptoms and cognitive impairments in schizophrenia: two key symptoms negatively influencing social functioning, Yonago Acta Med. 61 (2) (Jun. 2018) 91–102, https://doi.org/10.33160/yam.2018.06.001.

[3] S. Galderisi, A. Mucci, R.W. Buchanan, C. Arango, Negative symptoms of schizophrenia: new developments and unanswered research questions, Lancet Psychiatr. 5 (2018) 664–677, https://doi.org/10.1016/S2215-0366(18)30050-6.

[4] B. Kirkpatrick, R.W. Buchanan, D.E. Ross, W.T. Carpenter Jr., A separate disease within the syndrome of schizophrenia, Arch. Gen. Psychiatr. 58 (2) (2001) 165–171, https://doi.org/10.1001/archpsyc.58.2.165.

[5] P. Milev, B.C. Ho, S. Arndt, N.C. Andreasen, Predictive values of neurocognition and negative symptoms on functional outcome in schizophrenia: a longitudinal first-episode study with 7-year follow-up, Am. J. Psychiatr. 162 (3) (2005) 495–506, https://doi.org/10.1176/appi.ajp.162.3.495.

[6] G. Foussias, G. Remington, Negative symptoms in schizophrenia: avolition and Occam's razor, Schizophr. Bull. 36 (2) (2010) 359–369, https://doi.org/10.1093/schbul/sbn094.

[7] M. Carbon, C.U. Correll, Thinking and acting beyond the positive: the role of the cognitive and negative symptoms in schizophrenia, CNS Spectr. 19 (Suppl 1) (2014) 38–52, https://doi.org/10.1017/S1092852914000601, quiz 35–37, 53.

[8] C.U. Correll, N.R. Schooler, Negative symptoms in schizophrenia: a review and clinical Guide for recognition, assessment, and treatment, Neuropsychiatric Dis. Treat. 16 (2020 Feb 21) 519–534, https://doi.org/10.2147/NDT.S225643.

[9] E. Simonsen, G. Newton-Howes, Personality pathology and schizophrenia, Schizophr. Bull. 44 (6) (Oct. 2018) 1180–1184, https://doi.org/10.1093/schbul/sby053.

[10] B.T. Talreja, S. Shah, L. Kataria, Cognitive function in schizophrenia and its association with socio-demographics factors, Ind. Psychiatr. J. 22 (1) (Jan. 2013) 47–53, https://doi.org/10.4103/0972-6748.123619.

[11] B.F. O'Donnell, J.M. Swearer, L.T. Smith, P.G. Nestor, M.E. Shenton, R. W. McCarley, Selective deficits in visual perception and recognition in schizophrenia, Am. J. Psychiatr. 153 (5) (May 1996) 687–692, https://doi.org/10.1176/ajp.153.5.687.

[12] B.J. Miller, D.R. Goldsmith, Towards an immunophenotype of schizophrenia: progress, potential mechanisms, and future directions, Neuropsychopharmacology 42 (1) (Jan. 2017) 299–317, https://doi.org/10.1038/npp.2016.211.

[13] G.M. Beyene, G. Legas, T. Azale, M. Abera, S. Asnakew, The magnitude of disability in patients with schizophrenia in North West Ethiopia: a multicenter hospital-based cross-sectional study, Heliyon 7 (5) (May 2021) e07053, https://doi.org/10.1016/j.heliyon.2021.e07053.

[14] E. Barbotte, F. Guillemin, N. Chau, Lorhandicap Group, Prevalence of impairments, disabilities, handicaps and quality of life in the general population: a review of recent literature, Bull. World Health Organ. 79 (11) (2001) 1047–1055.

[15] S. Shamsi, et al., Cognitive and symptomatic predictors of functional disability in schizophrenia, Schizophr. Res. 126 (1–3) (Mar. 2011) 257–264, https://doi.org/10.1016/j.schres.2010.08.007.

[16] A.B. Gunnarsson, A.-K. Hedberg, C. Håkansson, K. Hedin, P. Wagman, Occupational performance problems in people with depression and anxiety, Scand. J. Occup. Ther. (Feb. 2021) 1–11, https://doi.org/10.1080/11038128.2021.1882562.

[17] F.J. Charlson, et al., Global epidemiology and burden of schizophrenia: findings from the global burden of disease study 2016, Schizophr. Bull. 44 (6) (Oct. 2018) 1195–1203, https://doi.org/10.1093/schbul/sby058.

[18] T. Halldorsdottir, E.B. Binder, Gene × environment interactions: from molecular mechanisms to behavior, Annu. Rev. Psychol. 68 (Jan. 2017) 215–241, https://doi.org/10.1146/annurev-psych-010416-044053.

[19] T. Liu, L. Zhang, L. Pang, N. Li, G. Chen, X. Zheng, Schizophrenia-related disability in China: prevalence, gender, and geographic location, Psychiatr. Serv. 66 (3) (Mar. 2015) 249–257, https://doi.org/10.1176/appi.ps.201400032.

[20] J. Rahul, D. Sharma, L.D. Sharma, U. Nanda, A.K. Sarkar, A systematic review of EEG based automated schizophrenia classification through machine learning and deep learning, Front. Hum. Neurosci. 18 (2024) 1347082, https://doi.org/10.3389/fnhum.2024.13470.

[21] A. Perrottelli, G.M. Giordano, F. Brando, L. Giuliani, A. Mucci, EEG-based measures in at-risk mental state and early stages of schizophrenia: a systematic review, Front. Psychiatr. 12 (May 2021) 653642, https://doi.org/10.3389/fpsyt.2021.653642.

[22] K.J. Friston, Dysfunctional connectivity in schizophrenia, World Psychiatr. 1 (2) (2002 Jun) 66–71. PMID: 16946855; PMCID: PMC1489874.

[23] E. Bleuler, Dementia Praecox or the Group of Schizophrenias, International Universities Press, New York, 1911.

[24] K. Friston, H.R. Brown, J. Siemerkus, K.E. Stephan, The dysconnection hypothesis (2016), Schizophr. Res. 176 (2–3) (2016 Oct) 83–94, https://doi.org/10.1016/j.schres.2016.07.014.

[25] J. Mukai, M. Tamura, K. Fenelon, A.M. Rosen, T.J. Spellman, R. Kang, A. B. MacDermott, M. Karayiorgou, J.A. Gordon, J.A. Gogos, Molecular substrates of altered axonal growth and brain connectivity in a mouse model of schizophrenia, Neuron 86 (2015) 680–695.

[26] K.E. Stephan, K.J. Friston, C.D. Frith, Dysconnection in schizophrenia: from abnormal synaptic plasticity to failures of self-monitoring, Schizophr. Bull. 35 (2009) 509–527.

[27] S. Cull-Candy, S. Brickley, M. Farrant, NMDA receptor subunits: diversity, development and disease, Curr. Opin. Neurobiol. 11 (2001) 327–335.

[28] T. Li LuiS, W. Deng, X. Huang, L. Jiang, X. Ma, H. Chen, T. Zhang, X. Li, D. Li, L. Zou, H. Tang, X.J. Zhou, A. Mechelli, D.A. Collier, J.A. Sweeney, T. Li, Q. GongAssociation, Of cerebral deficits with clinical symptoms in antipsychotic-naïve first-episode schizophrenia: an optimized voxel-based morphometry and resting state functional connectivity study, Am. J. Psychiatr. 166 (2009) 196–205.

[29] D.S. Bassett LynallME, R. Kerwin, P.J. McKenna, M. Kitzbichler, U. Muller, E. Bullmore, Functional connectivity and brain networks in schizophrenia, J. Neurosci. 30 (28) (2010) 9477–9487.

[30] S. Guo, Keith M. Kendrick, Jie Zhang, Matthew Broome, Rongjun Yu, Zhening Liu, Jianfeng Feng, Brain-wide functional inter-hemispheric disconnection is a potential biomarker for schizophrenia and distinguishes it from depression, Neuroimage: Clinical 2 (2013) 818–826, https://doi.org/10.1016/j.nicl.2013.06.008. ISSN 2213-1582.

[31] A.L. Wheeler, A.N. Voineskos, A review of structural neuroimaging in schizophrenia: from connectivity to connectomics, Front. Hum. Neurosci. 8 (2014) 653, https://doi.org/10.3389/fnhum.2014.00653.

[32] M. Dabiri, Firouzabadi F. Dehghani, K. Yang, P.B. Barker, R.R. Lee, D.M. Yousem, Neuroimaging in schizophrenia: a review article, Front. Neurosci. 16 (2022 Nov 15) 1042814, https://doi.org/10.3389/fnins.2022.1042814.

[33] S.I. Dimitriadis, Assessing the repeatability of multi-frequency multi-layer brain network topologies across alternative researcher's choice paths, Neuroinformatics 21 (1) (2023 Jan) 71–88, https://doi.org/10.1007/s12021-022-09610-6.

[34] M. Kubicki ChoiH, T.J. Whitford, J.L. Alvarado, D.P. Terry, M. Niznikiewicz, R. W. McCarley, J.S. Kwon, M.E. Shenton, Diffusion tensor imaging of anterior commissural fibers in patients with schizophrenia, Schizophr. Res. 130 (2011) 78–85.

[35] J.M.N. Duarte, L. Xin, Magnetic resonance spectroscopy in schizophrenia: evidence for glutamatergic dysfunction and impaired energy metabolism, Neurochem. Res. 44 (1) (2019 Jan) 102–116, https://doi.org/10.1007/s11064-018-2521-z.

[36] J.C. Edgar, A. Guha, G.A. Miller, Magnetoencephalography for schizophrenia, Neuroimaging Clin. 30 (2) (2020 May) 205–216, https://doi.org/10.1016/j.nic.2020.01.002.

[37] E. Olejarczyk, W. Jernajczyk, Graph-based analysis of brain connectivity in schizophrenia, PLoS One 12 (11) (Nov. 2017) e0188629, https://doi.org/10.1371/journal.pone.0188629.

[38] S.V. Borisov, A.Y. Kaplan, N.L. Gorbachevskaya, et al., Analysis of EEG structural synchrony in adolescents with schizophrenic disorders, Hum. Physiol. 31 (2005) 255–261, https://doi.org/10.1007/s10747-005-0042-z.

[39] J. Ford, V. Palzes, B. Roach, D. Mathalon, Did I do that? Abnormal predictive processes in schizophrenia when button pressing to deliver a tone, Schizophr. Bull. 40 (2014) 804–812, https://doi.org/10.1093/schbul/sbt072.

[40] M. Vázquez, A. Maghsoudi, I. Mariño, An interpretable machine learning method for the detection of schizophrenia using EEG signals, Front. Syst. Neurosci. 15 (2021) 652662, https://doi.org/10.3389/fnsys.2021.652662.

[41] M. Agarwal, A. Singhal, Fusion of pattern-based and statistical features for Schizophrenia detection from EEG signals, Med. Eng. Phys. 112 (2023) 103949, https://doi.org/10.1016/j.medengphy.2023.103949.

[42] E. Aydemir, S. Dogan, M. Baygin, C. Ooi, P. Barua, T. Tuncer, et al., CGP17Pat: automated schizophrenia detection based on a cyclic group of prime order patterns using EEG Signals, Healthcare 10 (2022) 643, https://doi.org/10.3390/healthcare10040643.

[43] V. Jahmunah, O.S. Lih, V. Rajinikanth, E. Ciaccio, K. Hao Cheong, N. Arunkumar, Automated detection of schizophrenia using nonlinear signal processing methods, Artif. Intell. Med. 100 (2019) 101698, https://doi.org/10.1016/j.artmed.2019.07.006.

[44] H. Najafzadeh, M. Esmaeili, S. Farhang, Y. Sarbaz, S. Rasta, Automatic classification of schizophrenia patients using resting-state EEG signals, Phys. Eng. Sci. Med. 44 (2021) 855–870, https://doi.org/10.1007/s13246-021-01038-7.

[45] S. Azizi, D. Hier, D. Wunsch, Schizophrenia classification using resting state EEG functional connectivity: source level outperforms sensor level, Annu. Int. Conf. IEEE Eng. Med. Biol. Soc. 2021 (2021) 1770–1773, https://doi.org/10.1109/EMBC46164.2021.9630713.

[46] K. Kim, N. Duc, M. Choi, B. Lee, EEG microstate features for schizophrenia classification, PLoS One 16 (2021) e0251842, https://doi.org/10.1371/journal.pone.0251842.

[47] A. Keihani, S. Sajadi, M. Hasani, F. Ferrarelli, Bayesian optimization of machine learning classification of resting-state EEG microstates in schizophrenia: a proof-of-concept preliminary study based on secondary analysis, Brain Sci. 12 (2022) 1497, https://doi.org/10.3390/brainsci12111497.

[48] S. Prabhakar, H. Rajaguru, S. Kim, Schizophrenia EEG signal classification based on swarm intelligence computing, Comput. Intell. Neurosci. 2020 (2020) 8853835, https://doi.org/10.1155/2020/8853835.
[49] M. Shen, P. Wen, B. Song, Y. Li, 3D convolutional neural network for schizophrenia detection using as EEG-based functional brain network, Biomed. Signal Process Control 89 (2024) 105815, https://doi.org/10.1016/j.bspc.2023.105815. ISSN 1746-8094.
[50] M. Shen, P. Wen, B. Song, Y. Li, Automatic identification of schizophrenia based on EEG signals using dynamic functional connectivity analysis and 3D convolutional neural network, Comput. Biol. Med. 160 (2023) 107022, https://doi.org/10.1016/j.compbiomed.2023.107022. ISSN 0010-4825.
[51] C. Phang, C. Ting, S.B. Samdin, H. Ombao, Classification of EEG-based effective brain connectivity in schizophrenia using deep neural networks, in: 2019 9th International IEEE/EMBS Conference on Neural Engineering, NER, 2019 401406, https://doi.org/10.1109/NER.2019.8717087.
[52] S. Khare, V. Bajaj, A hybrid decision support system for automatic detection of Schizophrenia using EEG signals, Comput. Biol. Med. 141 (2022) 105028, https://doi.org/10.1016/j.compbiomed.2021.105028.
[53] S. Khare, V. Bajaj, A self-learned decomposition and classification model for schizophrenia diagnosis, Comput. Methods Progr. Biomed. 211 (2021) 106450, https://doi.org/10.1016/j.cmpb.2021.106450.
[54] A. Aksöz, D. Akyüz, F. Bayir, N.C. Yildiz, F. Orhanbulucu, F. Latifoğlu, et al., Analysis and classification of schizophrenia using event related potential signals, Comput. Sci. 2022 (2022) 32–36, https://doi.org/10.1186/s40345-022-00258-4.
[55] K. Rajesh, T. Sunil Kumar, Schizophrenia detection in adolescents from EEG signals using symmetrically weighted local binary patterns, Annu. Int. Conf. IEEE Eng. Med. Biol. Soc. 2021 (2021) 963–966, https://doi.org/10.1109/EMBC46164.2021.9630232.
[56] C. Devia, R. Mayol-Troncoso, J. Parrini, G. Orellana, A. Ruiz, P. Maldonado, et al., EEG classification during scene free-viewing for schizophrenia detection, IEEE Trans. Neural Syst. Rehabil. Eng. 27 (2019) 1193–1199, https://doi.org/10.1109/TNSRE.2019.2913799.
[57] A. Neuhaus, F. Popescu, J. Bates, T. Goldberg, A. Malhotra, Single-subject classification of schizophrenia using event-related potentials obtained during auditory and visual oddball paradigms, Eur. Arch. Psychiatr. Clin. Neurosci. 263 (2013) 241–247, https://doi.org/10.1007/s00406-012-0326-7.
[58] M. Luján, J. Mateo Sotos, A. Torres, J. Santos, O. Quevedo, A. Borja, Mental disorder diagnosis from EEG signals employing automated leaning procedures based on radial basis functions, J. Med. Biol. Eng. 42 (2022) 853–859, https://doi.org/10.1007/s40846-022-00758-9.
[59] A. Zandbagleh, S. Mirzakuchaki, M. Daliri, P. Premkumar, S. Sanei, Classification of low and high schizotypy levels via evaluation of brain connectivity, Int. J. Neural Syst. 32 (2022) 2250013, https://doi.org/10.1142/S0129065722500137.
[60] X. Du, J. Li, D. Xiong, Z. Pan, F. Wu, Y. Ning, et al., [Research on electroencephalogram specifics in patients with schizophrenia under cognitive load], Sheng Wu Yi Xue Gong Cheng Xue Za Zhi 37 (2020) 45–53, https://doi.org/10.7507/1001-5515.201810007.
[61] J. Kim, H. Lee, S. Lee, EEG source network for the diagnosis of schizophrenia and the identification of subtypes based on symptom severity-a machine learning approach, J. Clin. Med. 9 (2020) 3934, https://doi.org/10.3390/jcm9123934.
[62] J. Jeong, T. Wendimagegn, E. Chang, Y. Chun, J. Park, H. Kim, et al., Classifying schizotypy using an audiovisual emotion perception test and scalp electroencephalography, Front. Hum. Neurosci. 11 (2017) 450, https://doi.org/10.3389/fnhum.2017.00450.
[63] H. Lai, J. Feng, Y. Wang, W. Deng, J. Zeng, T. Li, et al., [Resting-state electroencephalogram classification of patients with schizophrenia or depression], Sheng Wu Yi Xue Gong Cheng Xue Za Zhi 36 (2019) 916–923, https://doi.org/10.7507/1001-5515.201812041.
[64] G. Guo, Y. Zhao, C. Liu, Y. Fu, X. Xi, L. Jin, et al., Method for persistent topological features extraction of schizophrenia patients' electroencephalography signal based on persistent homology, Front. Comput. Neurosci. 16 (2022) 1024205, https://doi.org/10.3389/fncom.2022.1024205.
[65] L. Santos-Mayo, L. San-Jose-Revuelta, J.I.A. Arribas, Computer-aided diagnosis system with EEG Based on the P3b wave during an auditory odd-ball task in schizophrenia, IEEE Trans. Biomed. Eng. 64 (2016) 395–407, https://doi.org/10.1109/TBME.2016.2558824.
[66] M. Shim, H. Hwang, D. Kim, S. Lee, C. Im, Machine-learning-based diagnosis of schizophrenia using combined sensor-level and source-level EEG features, Schizophr. Res. 176 (2016) 314–319, https://doi.org/10.1016/j.schres.2016.05.007.
[67] Q. Chang, M. Liu, Q. Tian, H. Wang, Y. Luo, J. Zhang, C. Wang, EEG-based brain functional connectivity in first-episode schizophrenia patients, ultra-high-risk individuals, and healthy controls during P50 suppression, Front. Hum. Neurosci. 13 (2019) 379, https://doi.org/10.3389/fnhum.2019.00379.
[68] H. Wang, L.L. Zeng, Y. Chen, et al., Evidence of a dissociation pattern in default mode subnetwork functional connectivity in schizophrenia, Sci. Rep. 5 (2015) 14655, https://doi.org/10.1038/srep14655.
[69] K.-M. Choi, J.-Y. Kim, Y.-W. Kim, J.-W. Han, C.-H. Im, S.-H. Lee, Comparative analysis of default mode networks in major psychiatric disorders using resting-state EEG, Sci. Rep. 11 (1) (Nov. 2021) 22007, https://doi.org/10.1038/s41598-021-00975-3.
[70] S. Chevallier, M.-C. Corsi, F. Yger, F. De Vico Fallani, Riemannian geometry for combining functional connectivity metrics and covariance in BCI, Software Impacts 12 (May 2022) 100254, https://doi.org/10.1016/j.simpa.2022.100254.
[71] Y.W. Kim, Sungkean Kim, Miseon Shim, Min Jin Jin, Hyeonjin Jeon, Seung-Hwan Lee, Chang-Hwan Im, Riemannian classifier enhances the accuracy of machine-learning-based diagnosis of PTSD using resting EEG, Prog. Neuro Psychopharmacol. Biol. Psychiatr. 102 (2020) 109960, https://doi.org/10.1016/j.pnpbp.2020.109960. ISSN 0278-5846.
[72] K. You, H.-J. Park, Re-visiting Riemannian geometry of symmetric positive definite matrices for the analysis of functional connectivity, Neuroimage 225 (Jan. 2021) 117464, https://doi.org/10.1016/j.neuroimage.2020.117464.
[73] F. Yger, M. Berar, F. Lotte, Riemannian approaches in brain-computer interfaces: a review, IEEE Trans. Neural Syst. Rehabil. Eng. 25 (10) (Oct. 2017) 1753–1762, https://doi.org/10.1109/TNSRE.2016.2627016.
[74] G. Varoquaux, F. Baronnet, A. Kleinschmidt, P. Fillard, B. Thirion, Detection of brain functional-connectivity difference in post-stroke patients using group-level covariance modelling, Med. Image Comput. Comput. Assist Int. 13 (2010) 200–208.
[75] M. Rahim, B. Thirion, G. Varoquaux, Population shrinkage of covariance (PoSCE) for better individual brain functional-connectivity estimation, Med. Image Anal. 54 (2019) 138–148.
[76] Y. Gao, Xinyu Sun, Ming Meng, Yingchun Zhang, EEG emotion recognition based on enhanced SPD matrix and manifold dimensionality reduction, Comput. Biol. Med. 146 (2022) 105606, https://doi.org/10.1016/j.compbiomed.2022.105606. ISSN 0010 4825.
[77] F.P. Kalaganis, N.A. Laskaris, E. Chatzilari, S. Nikolopoulos, I. Kompatsiaris, A riemannian geometry approach to reduced and discriminative covariance estimation in brain computer interfaces, IEEE Trans. Biomed. Eng. 67 (1) (Jan. 2020) 245–255, https://doi.org/10.1109/TBME.2019.2912066.
[78] G.J. Székely, M.L. Rizzo, The distance correlation-test of independence in high dimension, J. Multivariate Anal. 117 (May 2013) 193–213, https://doi.org/10.1016/j.jmva.2013.02.012.
[79] A. Barachant, S. Bonnet, M. Congedo, C. Jutten, Multiclass brain-computer interface classification by Riemannian geometry, IEEE Trans. Biomed. Eng. 59 (4) (Apr. 2012) 920–928, https://doi.org/10.1109/TBME.2011.2172210.
[80] A.P. Shirokov, Structures on differentiable manifolds, in: R.V. Gamkrelidze (Ed.), Progress in Mathematics: Algebra and Geometry, Springer US, Boston, MA, 1971, pp. 137–207.
[81] W. Forstner, B. Moonen, A metric for covariance matrices, in: E.W. Grafarend, F. W. Krumm, V.S. Schwarze (Eds.), Geodesy-the Challenge of the 3rd Millennium, Springer-Verlag, Berli, 2003, pp. 299–309.
[82] X. Pennec, P. Fillard, N. Ayache, A riemannian framework for tensor computing, Int. J. Comput. Vis. 66 (1) (Jan. 2006) 41–66, https://doi.org/10.1007/s11263-005-3222-z.
[83] M. Moakher, A differential geometric approach to the geometric mean of symmetric positive-definite matrices, SIAM J. Matrix Anal. Appl. 26 (3) (2005) 735.
[84] P.T. Fletcher, S. Joshi, Principal geodesic analysis on symmetric spaces: statistics of diffusion tensors, in: Computer Vision and Mathematical Methods in Medical and Biomedical Image Analysis, Springer, 2004, pp. 87–98.
[85] K. You, H.-J. Park, Re-visiting Riemannian geometry of symmetric positive definite matrices for the analysis of functional connectivity, Neuroimage 225 (Jan. 2021) 117464, https://doi.org/10.1016/j.neuroimage.2020.117464.
[86] D.A. Bini, B. Iannazzo, Computing the Karcher mean of symmetric positive definite matrices, Linear Algebra Appl. 438 (4) (Feb. 2013) 1700–1710, https://doi.org/10.1016/j.laa.2011.08.052.
[87] S.I. Dimitriadis, Y. Sun, K. Kwok, N.A. Laskaris, N. Thakor, A. Bezerianos, Cognitive workload assessment based on the tensorial treatment of EEG estimates of cross-frequency phase interactions, Ann. Biomed. Eng. 43 (4) (2015 Apr) 977–989, https://doi.org/10.1007/s10439-014-1143-0.
[88] X. He, D. Cai, P. Niyogi, Tensor subspace analysis, in: Advances in Neural Information Processing Systems, 2005, pp. 499–506.
[89] S.I. Dimitriadis, Reconfiguration of αmplitude driven dominant coupling modes (DoCM) mediated by α-band in adolescents with schizophrenia spectrum disorders, Prog. Neuro-Psychopharmacol. Biol. Psychiatry 108 (Jun. 2021) 110073, https://doi.org/10.1016/j.pnpbp.2020.110073.
[90] A. Delorme, S. Makeig, EEGLAB: an open source toolbox for analysis of single-trial EEG dynamics including independent component analysis, J. Neurosci. Methods 134 (1) (Mar. 2004) 9–21, https://doi.org/10.1016/j.jneumeth.2003.10.009.
[91] V.S. Fonov, et al., Unbiased average age-appropriate atlases for pediatric studies, Neuroimage 54 (1) (Jan. 2011) 313–327, https://doi.org/10.1016/j.neuroimage.2010.07.033.
[92] V.S. Fonov, A.C. Evans, R.C. McKinstry, C.R. Almli, D.L. Collins, Unbiased nonlinear average age-appropriate brain templates from birth to adulthood, Neuroimage 47 (Jul. 2009) S102, https://doi.org/10.1016/S1053-8119(09)70884-5.
[93] F. Tadel, S. Baillet, J.C. Mosher, D. Pantazis, R.M. Leahy, Brainstorm: a user-friendly application for MEG/EEG analysis, Comput. Intell. Neurosci. 2011 (Apr. 2011) 879716, https://doi.org/10.1155/2011/879716.
[94] R.D. Pascual-Marqui, Standardized low-resolution brain electromagnetic tomography (sLORETA): technical details, Methods Find. Exp. Clin. Pharmacol. 24 (2002) 5–12. Suppl D.
[95] R.S. Desikan, et al., An automated labeling system for subdividing the human cerebral cortex on MRI scans into gyral based regions of interest, Neuroimage 31 (3) (Jul. 2006) 968–980, https://doi.org/10.1016/j.neuroimage.2006.01.021.
[96] S.I. Dimitriadis, Assessing the repeatability of multi-frequency multi-layer brain network topologies across alternative researcher's choice paths, Neuroinformatics 21 (2023) 71–88, https://doi.org/10.1007/s12021-022-09610-6.
[97] M. Shim, H. Hwang, D. Kim, S. Lee, C. Im, Machine-learning-based diagnosis of schizophrenia using combined sensor-level and source-level EEG features,

Schizophr. Res. 176 (2016) 314–319, https://doi.org/10.1016/j.schres.2016.05.007.
[98] A. Yamin, M. Dayan, L. Squarcina, P. Brambilla, V. Murino, V. Diwadkar, D. Sona, Comparison of brain connectomes using geodesic distance on manifold:a twin study, in: 2019 IEEE 16th International Symposium on Biomedical Imaging (ISBI 2019), 2019, pp. 1797–1800. Venice, Italy.
[99] C.E. Ginestet, J. Li, P. Balachandran, S. Rosenberg, E.D. Kolaczyk, Hypothesis testing for network data in functional neuroimaging, Ann. Appl. Stat. 11 (2017) 725–750.
[100] A. Davoudi, S.S. Ghidary, K. Sadatnejad, Dimensionality reduction based on distance preservation to local mean for symmetric positive definite matrices and its application in brain-computer interfaces, J. Neural. Eng. 14 (2017). Article 036019.
[101] X. Xie, Z.L. Yu, H. Lu, Z. Gu, Y. Li, Motor imagery classification based on bilinear sub-manifold learning of symmetric positive-definite matrices, IEEE Trans. Neural Syst. Rehabil. Eng. 25 (2017) 504–516.
[102] F. Li, Y. Xia, F. Wang, D. Zhang, X. Li, F. He, Transfer learning algorithm of P300-EEG signal based on XDAWN spatial filter and riemannian geometry classifier, Appl. Sci. 10 (5) (Mar. 2020) 1804, https://doi.org/10.3390/app10051804.
[103] P. Zanini, M. Congedo, C. Jutten, S. Said, Y. Berthoumieu, Transfer learning: a riemannian geometry framework with applications to brain-computer interfaces, IEEE Trans. Biomed. Eng. 65 (5) (May 2018) 1107–1116, https://doi.org/10.1109/TBME.2017.2742541.
[104] S. Fiori, Visualization of Riemannian-manifold-valued elements by multidimensional scaling, Neurocomputing 74 (6) (Feb. 2011) 983–992, https://doi.org/10.1016/j.neucom.2010.11.015.
[105] F.P. Kalaganis, N.A. Laskaris, E. Chatzilari, D.A. Adamos, S. Nikolopoulos, I. Kompatsiaris, A complex-valued functional brain connectivity descriptor amenable to Riemannian geometry, J. Neural. Eng. 17 (2) (Apr. 2020) 24001, https://doi.org/10.1088/1741-2552/ab8130.
[106] K. Georgiadis, F.P. Kalaganis, V.P. Oikonomou, S. Nikolopoulos, N.A. Laskaris, I. Kompatsiaris, Rneumark: a riemannian EEG analysis framework for neuromarketing, Brain Inform 9 (1) (Sep. 2022) 22, https://doi.org/10.1186/s40708-022-00171-7.
[107] K. You, H.-J. Park, Geometric learning of functional brain network on the correlation manifold, Sci. Rep. 12 (1) (Oct. 2022) 17752, https://doi.org/10.1038/s41598-022-21376-0.
[108] G. Simeon, G. Piella, O. Camara, D. Pareto, Riemannian geometry of functional connectivity matrices for multi-site attention-deficit/hyperactivity disorder data harmonization, Front. Neuroinf. 16 (May 2022) 769274, https://doi.org/10.3389/fninf.2022.769274.
[109] M. Congedo, A. Barachant, R. Bhatia, Riemannian geometry for EEG-based brain-computer interfaces; a primer and a review, Brain-Computer Interfaces 4 (3) (Jul. 2017) 155–174, https://doi.org/10.1080/2326263X.2017.1297192.
[110] C. Simar, et al., Hyperscanning EEG and classification based on riemannian geometry for festive and violent mental state discrimination, Front. Neurosci. 14 (Dec. 2020) 588357, https://doi.org/10.3389/fnins.2020.588357.
[111] K.J. Friston, C.D. Frith, P.F. Liddle, R.S.J. Frackowiak, Functional connectivity—the principal-component analysis of large (pet) data sets, J. Cerebr. Blood Flow Metabol. 13 (1) (1993) 5–14.
[112] M.D. Fox, M.E. Raichle, Spontaneous fluctuations in brain activity observed with functional magnetic resonance imaging, Nat. Rev. Neurosci. 8 (9) (2007) 700–711.
[113] D. Rocca, P. Campisi, B. Vegso, P. Cserti, G. Kozmann, F. Babiloni, F.V. Fallani, Human brain distinctiveness based on EEG spectral coherence connectivity, IEEE Trans. Biomed. Eng. 61 (9) (2014 Sep) 2406–2412, https://doi.org/10.1109/TBME.2014.2317881.
[114] J. da Silva Castanheira, H.D. Orozco Perez, B. Misic, et al., Brief segments of neurophysiological activity enable individual differentiation, Nat. Commun. 12 (2021) 5713, https://doi.org/10.1038/s41467-021-25895-8.
[115] Maliheh Miri, Vahid Abootalebi, Enrico Amico, Hamid Saeedi-Sourck, Dimitri Van De Ville, Hamid Behjat, Graph learning from EEG data improves brain fingerprinting compared to correlation-based connectomes, Science Talks 10 (2024) 100330, https://doi.org/10.1016/j.sctalk.2024.100330. ISSN 2772-5693.
[116] D. Van De Ville, Y. Farouj, M.G. Preti, R. Liégeois, E. Amico, When makes you unique: temporality of the human brain fingerprint, Sci. Adv. 7 (42) (2021 Oct 15) eabj0751, https://doi.org/10.1126/sciadv.abj0751.
[117] S.I. Dimitriadis, B. Routley, D.E.J. Linden, K.D. Singh, Multiplexity of human brain oscillations as a personal brain signature, Hum. Brain Mapp. 44 (17) (2023 Dec 1) 5624–5640, https://doi.org/10.1002/hbm.26466.
[118] M.E. Raichle, A.M. MacLeod, A.Z. Snyder, W.J. Powers, D.A. Gusnard, G. L. Shulman, A default mode of brain function, Proc. Natl. Acad. Sci. U.S.A. 98 (2) (2001) 676–682.
[119] R.L. Buckner, J.R. Andrews-Hanna, D.L. Schacter, The brain's default network - anatomy, function, and relevance to disease, Year in Cognitive Neuroscience 1124 (2008) 1–38.
[120] J.R. Andrews-Hanna, J. Smallwood, R.N. Spreng, The default network and self-generated thought: component processes, dynamic control, and clinical relevance, Ann. N. Y. Acad. Sci. 1326 (5) (2014) 29–52.
[121] M.D. Greicius, B. Krasnow, A.L. Reiss, V. Menon, Functional connectivity in the resting brain: a network analysis of the default mode hypothesis, Proc. Natl. Acad. Sci. U. S. A. 100 (2003) 253–258.
[122] G.E. Doucet, W.H. Lee, S. Frangou, Evaluation of the spatial variability in the major resting-state networks across human brain functional atlases, Hum. Brain Mapp. 40 (2019) 4577–4587.
[123] B.T. Yeo, F.M. Krienen, J. Sepulcre, M.R. Sabuncu, D. Lashkari, M. Hollinshead, et al., The organization of the human cerebral cortex estimated by intrinsic functional connectivity, J. Neurophysiol. 106 (2011) 1125–1165.
[124] J.S. Damoiseaux, S.A. Rombouts, F. Barkhof, P. Scheltens, C.J. Stam, S.M. Smith, et al., Consistent resting-state networks across healthy subjects, Proc. Natl. Acad. Sci. U. S. A. 103 (2006) 13848–13853.
[125] T. Meindl, S. Teipel, R. Elmouden, S. Mueller, W. Koch, O. Dietrich, et al., Test-retest reproducibility of the default-mode network in healthy individuals, Hum. Brain Mapp. 31 (2010) 237–246.
[126] R. Marchitelli, O. Collignon, J. Jovicich, Test–retest reproducibility of the intrinsic default mode network: influence of functional magnetic resonance imaging slice-order acquisition and head-motion correction methods, Brain Connect. 7 (2017) 69–83.
[127] R.N. Spreng, R.A. Mar, A.S. Kim, The common neural basis of autobiographical memory, prospection, navigation, theory of mind, and the default mode: a quantitative meta-analysis, J. Cognit. Neurosci. 21 (2009) 489–510.
[128] D.A. Gusnard, E. Akbudak, G.L. Shulman, M.E. Raichle, Medial prefrontal cortex and self-referential mental activity: relation to a default mode of brain function, Proc. Natl. Acad. Sci. U.S.A. 98 (2001) 4259–4264.
[129] D.L. Schacter, D.R. Addis, R.L. Buckner, Remembering the past to imagine the future: the prospective brain, Nat. Rev. Neurosci. 8 (2007) 657–661.
[130] K.C. Fox, R.N. Spreng, M. Ellamil, J.R. Andrews-Hanna, K. Christoff, The wandering brain: meta-analysis of functional neuroimaging studies of mind-wandering and related spontaneous thought processes, Neuroimage 111 (2015) 611–621.
[131] M. Greicius, Resting-state functional connectivity in neuropsychiatric disorders, Curr. Opin. Neurol. 21 (2008) 424–430.
[132] K. Jerbi, J.R. Vidal, T. Ossandon, S.S. Dalal, J. Jung, D. Hoffmann, L. Minotti, O. Bertrand, P. Kahane, J.P. Lachaux, Exploring the electrophysiological correlates of the default-mode network with intracerebral EEG, Front. Syst. Neurosci. 4 (2010 Jun 28) 27, https://doi.org/10.3389/fnsys.2010.00027.
[133] R.T. Toll, W. Wu, S. Naparstek, Y. Zhang, M. Narayan, B. Patenaude, C. De Los Angeles, K. Sarhadi, N. Anicetti, P. Longwell, E. Shpigel, R. Wright, J. Newman, B. Gonzalez, R. Hart, S. Mann, D. Abu-Amara, K. Sarhadi, C. Cornelssen, C. Marmar, A. Etkin, An electroencephalography connectomic profile of posttraumatic stress disorder, Am. J. Psychiatr. 177 (3) (2020 Mar 1) 233–243, https://doi.org/10.1176/appi.ajp.2019.18080911.
[134] Z. Sha, T.D. Wager, A. Mechelli, Y. He, Common dysfunction of large-scale neurocognitive networks across psychiatric disorders, Biol. Psychiatr. 85 (2019) 379–388.
[135] J.R. Andrews-Hanna, K. Christoff, M.F. O'Connor, Dynamic regulation of internal experience, in: R. Lane, L. Ryan, L. Nadel (Eds.), The Neuroscience of Enduring Change: the Neural Basis of Talk Therapies, Oxford University Press, New York, NY, 2019.
[136] M.L. Hu, X.F. Zong, J.J. Mann, J.J. Zheng, Y.H. Liao, Z.C. Li, et al., A review of the functional and anatomical default mode network in schizophrenia, Neurosci. Bull. 33 (2017) 73–84.
[137] A.G. Garrity, et al., Abberant 'default mode' functional connectivity in schizophrenia, Am. J. Psychiatr. 164 (2007) 450–457.
[138] Y.I. Sheline, D.M. Barch, J.L. Price, M.M. Rundle, S.N. Vaishnavi, A.Z. Snyder, M. A. Mintun, S. Wang, R.S. Coalson, M.E. Raichle, The default mode network and self-referential processes in depression, Proc. Natl. Acad. Sci. U. S. A. 106 (6) (2009 Feb 10) 1942–1947, https://doi.org/10.1073/pnas.0812686106.
[139] S. Passow, K. Specht, T.C. Adamsen, M. Biermann, N. Brekke, A.R. Craven, L. Ersland, R. Grüner, N. Kleven-Madsen, O.H. Kvernenes, T. Schwarzlmüller, R. A. Olesen, K. Hugdahl, Default-mode network functional connectivity is closely related to metabolic activity, Hum. Brain Mapp. 36 (6) (2015 Jun) 2027–2038, https://doi.org/10.1002/hbm.22753.
[140] B. Nelson, T.J. Whitford, S. Lavoie, L.A. Sass, What are the neurocognitive correlates of basic self-disturbance in schizophrenia?: integrating phenomenology and neurocognition. Part 2 (Aberrant salience), Schizophr. Res. 152 (2014) 12–19.
[141] O. Meiron, Self-awareness in schizophrenia: identifying common neural oscillatory parameters underlying altered sense of self-agency and reduced prefrontal cortex excitability, Current Opinion in Behavioral Sciences 58 (2024) 101398, https://doi.org/10.1016/j.cobeha.2024.101398. ISSN 2352-1546.
[142] S. Iglesias-Parro, M.F. Soriano, M. Prieto, I. Rodríguez, J.I. Aznarte, A.J. Ibáñez-Molina, Introspective and neurophysiological measures of mind wandering in schizophrenia, Sci. Rep. 10 (2020) 4833.
[143] D.J. Shin, T.Y. Lee, W.H. Jung, S.N. Kim, J.H. Jang, J.S. Kwon, Away from home: the brain of the wandering mind as a model for schizophrenia, Schizophr. Res. 165 (2015) 83–89.
[144] S. Iglesias-Parro, M.F. Soriano, A.J. Ibáñez-Molina, A.V. Pérez-Matres, J. Ruiz de Miras, Examining neural connectivity in schizophrenia using task-based EEG: a graph theory approach, Sensors 23 (2023) 8722, https://doi.org/10.3390/s23218722.
[145] J. Pripfl, R. Neumann, U. Köhler, C. Lamm, Effects of transcranial direct current stimulation on risky decision making are mediated by 'hot'and 'cold'decisions, personality, and hemisphere, Eur. J. Neurosci. 38 (2013) 3778–3785.
[146] S.D. Washington, J.W. VanMeter, Anterior-posterior connectivity within the default mode network increases during maturation, Int. J. Med. Biol. Front. 21 (2) (2015) 207–218.

[147] S. Marek, B. Tervo-Clemmens, F.J. Calabro, et al., Reproducible brain-wide association studies require thousands of individuals, Nature 603 (2022) 654–660, https://doi.org/10.1038/s41586-022-04492-9.
[148] P. Prado, J.A. Mejía, A. Sainz-Ballesteros, A. Birba, S. Moguilner, R. Herzog, M. Otero, J. Cuadros, L. Z-Rivera, D.F. O'Byrne, M. Parra, A. Ibáñez, Harmonized multi-metric and multi-centric assessment of EEG source space connectivity for dementia characterization, Alzheimers Dement (Amst) 15 (3) (2023 Jul 8) e12455, https://doi.org/10.1002/dad2.12455.
[149] S.I. Dimitriadis, Universal lifespan trajectories of source-space information flow extracted from resting-state MEG data, Brain Sci. 12 (10) (2022 Oct 18) 1404, https://doi.org/10.3390/brainsci12101404.